SUPER RESOLUTION MAPPING OF UAV IMAGES OF FARM FIELDS

ADEGOKE IGE ALADEBOYEJE
March, 2014

SUPERVISORS:
Prof. Dr. Ir. Alfred Stein
Dr. Valentyn Tolpekin

SUPER RESOLUTION MAPPING OF UAV IMAGES OF FARM FIELDS

ADEGOKE IGE ALADEBOYEJE
Enschede, The Netherlands, March, 2014

Thesis submitted to the Faculty of Geo-Information Science and Earth Observation of the University of Twente in partial fulfilment of the requirements for the degree of Master of Science in Geo-information Science and Earth Observation.
Specialization: Geoinformatics

SUPERVISORS:
Prof. Dr. Ir. Alfred Stein
Dr. Valentyn Tolpekin

THESIS ASSESSMENT BOARD:
Prof. Dr. Ir. M. G. Vosselman (Chair)
Dr. Ing. G. Polder (External Examiner, Wageningen UR)

ABSTRACT

Hyperspectral remote sensing data offers great advantages in crop monitoring. To this end, hyperspectral vegetation indices have been developed to extract bio physical and biochemical parameters from plants. Although some indices have been designed to minimise soil background effects, problem still exist because algorithms use the entire pixel and do not discriminate for mixtures at sub pixel scales. Remote sensing signals, in a farm field may include vegetation, soil and shadow components or other types of vegetation, all of which lead to inaccuracies in vegetation indices used for estimating crop parameters.

This study focuses mainly on developing a MRF based super resolution analysis for predicting canopy reflectance in farm field from UAV hyperspectral image (1m) at a high resolution. For the setup in this study, prior knowledge of the field was incorporated in defining the SR image grid. A thorough analysis of the intersection of pixels in the coarse and fine images was performed based on analysis of the footprint polygons. The relationship between the two images was established. SA was employed to find the minimum energy solution that corresponds to optimal SR image.

Experiment with parameter optimisation shows that smoothness parameter value of 0.7, initial temperature of 3, and updating schedule of 0.97 produced a reflectance image of canopy with high accuracy. The SR canopy reflectance image was compared to canopy spectral measurement from the field. Result shows a RMSE of 0.04. Further this study examines relationship between indices (e.g. NDRE, Chl red edge, REP, TCARI) computed from super resolution image and insitu measurement. By comparing their coefficients of determination R^2 strong relationship were found (REP 0.84, TCARI, CLrededge 0.87, and TCARI/OSAVI 0.91). Others gave weak relation (NDRE 0.41, CIgreen 0.55, and OSAVI 0.06)

ACKNOWLEDGEMENTS

All thanks to Almighty God for successful completion of this thesis.

I express appreciation to my supervisors Prof. Dr. Alfred Stein and Dr. Valentyn Tolpekin for their continuous encouragement, guidance and suggestions throughout the research period.

For the opportunity given to me to study at ITC I greatly appreciate NDDC and my parents Chief and Mrs Aladeboyeje for sponsorship

I am also very grateful to Dr. Kooistra of Wageningen University for his contributions and particularly for providing me data.

I appreciate the contribution of my friends; Gregory Ajibolade, Peter Fosudo, Sam Odu Joseph Ataguba, Birane Dia, Raja and Samson Kolade for their invaluable contributions.

Finally, I appreciate my siblings Ayodeji, Christianah Hannah, Segun, Joshua and Sarah for their encouragement and prayers. May God bless you all.

TABLE OF CONTENTS

LIST OF FIGURES

LIST OF TABLES

1. INTRODUCTION

1.1. Motivation and problem statement

The increase in food demand and energy as a result of the growing world population is a major challenge facing the agricultural sector (Liu et al., 2010). To produce enough yields to feed the world population, both the increase of economic returns and the reduction of input as well as protection of the environment have led the agricultural sector to develop a new generation of sustainable agricultural systems. Precision agriculture (PA) is a management strategy to optimize agriculture production. It uses information technology to bring together data from multiple data sources, for making decisions on crop production and crop growth aspects (National Research Council, 1997). In general, PA combines several technologies such as variable rate technologies (VRT), global positioning system (GPS), geographical information systems (GIS) and remote sensing (RS) to assist farmers in visualizing, analysing and managing the variability in crop yield and performance on site specific manner. Remote sensing technologies have been used in PA applications for instance, to identify the types of crops, examine variability in crop performance and management (Bala and Islam, 2009), determine crop status and response to pest and diseases (Hatfield and Prueger, 2010).

Timely assessment of crop growth conditions and early monitoring on every stage of growth is essential to increase agricultural productivity (Liu et al., 2010). The most important and major limiting factor for crop growth and productivity is chlorophyll content which is indirectly related to nitrogen content (Haboudane et al., 2002). Thus, there is a need for timely assessment of crop status in order to optimize yield and quality (Wu et al., 2007). Remote sensing methods have proven to be effective in estimating nitrogen and other crop growth-status indicators (Clevers and Kooistra, 2012). Most importantly, multispectral high resolution images allow for computation of vegetation indices (VIs) based on their broad spectral bands in evaluating biophysical properties such as leaf area index (LAI), Nitrogen content, crop canopy cover and Chlorophyll content at the field scale (Cetin et al., 2005; Jain et al., 2007; Lelong et al., 1998). Studies have shown that broad band multispectral data are inadequate for the remote sensing of vegetation biochemical properties and that narrow band (high spectral resolution; usually a bandwidth of 10 nm or less) hyperspectral data are required (Broge and Mortensen, 2002; Haboudane et al., 2004).

Unmanned Aerial Vehicles (UAVs) have proven to provide a flexible intermediate observation platform between satellite and manned aircraft that could improve continuous aspect of data acquisition at a local scale. Recent studies have highlighted the benefit of UAVs for small scale crop mapping and monitoring (Berni et al., 2009; Rango et al., 2009). A hyperspectral sensor on board a UAV can provide the required

narrow spectral band and high spatial resolution for site-specific nutrient management. Hyperspectral remote sensing data have the potential to detect more variations on vegetation than multispectral data, because these sensors use narrow spectral channels of less than 10 nm (Stagakis et al., 2010). The large division of channels allows for a selection of bands that provides the greatest contribution of data help in providing better identification of crops and exploitation of intra-field variation (homogenous fields), thereby providing improvement on crop management practices.

The continuously growing availability of hyperspectral imagery, recording hundreds of images corresponding to different wavelength channels, has opened new possibilities in the field of image analysis and classification (Landgrebe, 2005). In particular, hard classification algorithms have shown remarkable performance when dealing with pure pixels (Melgani and Bruzzone, 2004). In high resolution images, however, the spatial frequency of specific land cover classes may result in a large number of mixed pixels (Aplin and Atkinson, 2001). Thus, hard classification methods may not be appropriate for identifying and classifying farm fields. Sub-pixel classification like spectral unmixing are found to be more appropriate in classifying mixed pixels (Hu et al., 1999). The result of sub-pixel classification is a set of fraction images, each describing the proportion of a particular land cover class within a pixel.

Super resolution mapping (SRM) has been used as a method of classification, that considers the spatial distribution of class proportions within pixels (Atkinson, 1997). It generates maps of a finer resolution than that of the input image. SRM methods include Hopfield neural networks (Tatem et al., 2001), linear optimization methods (Verhoeye and De Wulf, 2002), genetic algorithms (Mertens et al., 2003), and Markov random fields (Kasetkasem et al., 2005; Poudyal, 2013). These techniques except Markov random field (MRF) depend upon the availability of an accurate sup-pixel classification. MRF is a contextual and probabilistic method that has been applied for the various image processing tasks such as image classification, segmentation and change detection (Tso and Mather, 2001).

1.2. Research identification

Poudyal (2013) explored the possibilities of MRF based SRM as a contextual classifier for identification of row crop structure for a potato field from VHR WorldView-2 image of 2 m resolution. Findings from the study proved that SRM with high emphasis on spatial contextual information from prior model and spectral information from imagery was able to detect row structure prominently even for relatively complex scenes with high mixed pixels. SRM result was further integrated with NDVI to account for spatial variation in crop status within the field. However, this study was made for relatively small area that contains small variation in NDVI values and validation of results was limited. To examine variability in the field, multi-spectral images are subjected to limitations of spectral resolution compared to hyperspectral images of narrow bands. In the site-specific nutrient management, NDVI has been found to saturate at

higher vegetation indices and invariable at low densities (Haboudane et al., 2004). Hence, there is need to explore other vegetation indices to characterize the variation in plants within the field.

Recent studies have demonstrated the usefulness of vegetation indices (VIs) derived from spectral reflectance of images in estimating crop biophysical and biochemical parameters such as leaf area index, biomass, leaf chlorophyll content and Nitrogen, (Clevers and Kooistra, 2012; Hatfield and Prueger, 2010; Navarro-Cerrillo et al., 2014). Problems with VIs remain, however, because algorithms use the entire pixel and do not discriminate for mixtures at sub-pixel scales. Remote sensing signals, in a farm field may include vegetation, soil and shadow components or other types of vegetation (e.g. weeds), all of which lead to inaccuracies in vegetation indices used for estimating crop parameters.
The idea is that the current study could provide farmers with valuable information to allow estimation of crop yield potential, exploration of spatial variability in plant health and to make decisions on proper nutrient management.

1.2.1. Research objectives

The aim of this research is to explore the possibility of retrieving crop parameters from hyperspectral image using MRF based super resolution analysis.
It includes the following sub- objectives:

- Estimate reflectance of canopy from the hyperspectral image using MRF and super resolution analysis.
- Derive hyperspectral vegetation indices (HVIs) that are sensitive to chlorophyll content as reported in literature.
- Investigate relationship between HVIs derived from in situ measurement and hyperspectral image.

1.2.2. Research questions

- Is it possible to predict canopy reflectance using MRF and super resolution analysis?
- What are the optimal parameter settings to obtain the best result?
- How can the results of super resolution be validated?
- Is there any relationship between HVIs derived from field measurement and super resolution image?

2. LITERATURE REVIEW

In this chapter, a review of the literature relevant to this thesis is given. The first section refers to broader research context of hyperspectral vegetation indices in the context of precision agriculture. Other areas covered are spectral unmixing for class area proportion estimation, super resolution mapping and Markov random field based super resolution mapping.

2.1. Hyperspectral vegetation indices (HVIs)

Spectral vegetation indices are mathematical combinations of different spectral bands mostly in the visible and near infrared regions of the electromagnetic spectrum. They are designed to enhance the vegetation signal while minimizing the error associated with atmospheric conditions, soil background effects, sensor geometry and solar illumination (Quintano et al., 2012).Though they can be computed for both multispectral and hyperspectral data, hyperspectral vegetation indices (HVIs) have a wider range than multispectral data and they offer a greater opportunity in finding the right index to predict specific biophysical or biochemical variable. Huete (1988) concluded that a strong relationship with crop characteristics is located in specific narrow bands in the longer wavelength portion of the red, in the shorter wavelength portion of green, in one particular section of the near-infrared, and in the moisture sensitive NIR. The study recommended 12 narrow bands in the 350 nm to 1050 nm range of the spectrum for optimum estimation of agricultural crop biochemical and biophysical properties.

The usefulness of the vegetation indices to assess crop status is different depending on the wavebands used for its derivation. This implies that for monitoring various properties of crops, different vegetation indices are required. To date, several indices have been developed in terms of their sensitivity to biophysical and biochemical properties such as LAI, Nitrogen content, canopy cover and Chlorophyll content. NDVI being a commonly used index related to the physical properties of vegetation canopy, LAI, percent crop cover, vegetation condition and biomass tends to saturate under high canopy coverage (Li Miao et al 2009). To overcome this, vegetation indices developed in the point of maximum slope in vegetation reflectance spectra (between wavelengths of 680-750nm) called Red-edge position have become promising (Clevers, 1989).

Gitelson et al. (2006) introduced the Modified Chlorophyll Absorption Reflectance Index (MCARI) to reduce the combined effect of non-photosynthetic parts and soil background. Haboudane et al. (2002) found that non photosynthetic elements still have effect on vegetation signal at low chlorophyll concentrations and proposed the Transformed Chlorophyll Absorption Reflectance Index (TCARI). Huete (1988) introduced the Soil Adjusted Vegetation Indices (SAVI) in the soil-line vegetation indices to account for the optical soil properties on the plant canopy. Other modifications include the Transformed

Soil Adjusted Vegetation Index (TSAVI), and Optimized Soil Adjusted Vegetation Index OSAVI (Rondeaux et al., 1996).

For the purpose of this research, hyperspectral spectral indices (*Table 2.1)* recommended in Clevers and Kooistra (2012) for determining chlorophyll content of the leaf were derived from both Cropscan spectral reflectance measurement and the hyperspectral data cube.

Index	Name	Formula	References
REP	Red edge position	$700 + 40\,(R_x - R_{700})/(R_{740} - R_{700})$ $R_x = (R_{670} - R_{780})/2$	(Guyot and Baret, 1988)
TCARI	Transformed chlorophyll absorption in reflectance index	$3[(R_{700} - R_{670})$ -0.2 $(R_{700} - R_{550})$ $(R_{700}/R_{670})]$	(Haboudane et al., 2002)
OSAVI	Optimized Soil-Adjusted Vegetation Index	$1.16(R_{800} - R_{670})/(R_{800} + R_{670} + 0.16)$	(Rondeaux et al., 1996)
TCARI /OSAVI	TCARI with Optimized Soil-Adjusted Vegetation Index	$3[(R_{700} - R_{670})-0.2\,(R_{700} - R_{550})\,(R_{700}/R_{670})]/$ $1.16(R_{800} - R_{670})\,/(R_{800}+R_{670}+0.16)$	(Haboudane et al., 2002)
$CI_{red\ edge}$	Chlorophyll Red Edge	$\left(\frac{R_{780}}{R_{710}}\right) - 1$	(Gitelson et al., 2006)
CI_{green}	Chlorophyll Green	$\left(\frac{R_{780}}{R_{550}}\right) - 1$	(Gitelson et al., 2006)
NDRE	Normalized Difference Red Edge Index	$(R_{780} - R_{740})/(R_{780} + R_{740})$	(Eitel et al., 2010)

Table 2.1: Vegetation indices evaluated in this study. Modified from:(Clevers and Kooistra, 2012)

2.2. Spectral Unmixing for class area estimation

A variety of methods is available to classify mixed pixels. Usually these methods estimate the fraction of each class in one pixel (Foody and Mathur, 2006). Spectral unmixing is a method by which the measured spectrum of mixed pixels is decomposed into a collection of constituent spectra, or endmembers, and a set of corresponding abundances that indicate the proportion of each endmember is present in the pixel (Keshava, 2003). The linear mixing model assumes that each ground cover only produces a single radiance and that the mixed spectrum is a linear combination of endmembers spectra (Zhu, 2005). The mixed model is defined by (Keshava, 2003):

$$x_i = \sum_{j=1}^{K} A_{ij} e_j + \varepsilon_i \,, j = 1, \dots K \qquad (1)$$

Where x_i is the spectral value of the actual image at pixel i, K is the total number of classes (endmembers), is the j^{th} endmember (i.e. is a $1 \times N$ vector, where N is the total number of bands), A_{ij} is

the proportion of class j at pixel i and ε_i is the error term. The class compositions must satisfy the following constraint:

$$\sum_{j=1}^{K} A_{ij} = 1, \qquad A_{ij} \geq 0, j = 1, \ldots\ldots\ldots K \tag{2}$$

Details on the mathematical concept of this technique are discussed in chapter 4 of this study.

Singular Value Decomposition (SVD) for Linear Unmixing

A Singular Value Decomposition (SVD) is a well-known Eigen analysis method of decomposing a matrix. For an arbitrary matrix X , the SVD of the matrix equals:

$$X = USV'$$

Where U is a $n \times n$ identical matrix, S is a $m \times n$ diagonal matrix having non negative real numbers on the diagonal and V'(the transpose of V) is a $m \times m$ unitary matrix. The diagonal entries of S are referred to as the singular values of X.

For pixel unmixing, Herries et al. (1996), used the SVD successfully in conjunction with key-vector analysis to extract end-member information from multispectral data with accuracies of 95%.

2.3. Super resolution mapping

Super resolution mapping is a technique that produces maps of a finer resolution than that of the input image. SRM considers the spatial distribution of class proportions within pixels. Tatem et al. (2001) applied Hopfield neural network algorithm as an energy minimization tool for fuzzy classification, presenting the spatial distribution of classes between pixels for simulated imagery. In Tatem et al. (2003), this algorithm was applied on Landsat TM data, their results showing that SRM with Hopfield neural networks produced higher accuracy compared to the other techniques using proportion image alone. They concluded that Hopfield neural network is a useful tool for identifying land cover from images at subpixel scale.

A linear optimization technique for sub-pixel mapping was proposed in Verhoeye and De Wulf (2002). In their study, coarse resolution images were used. If the main assumption on spatial dependency holds, however, the technique can also be applied on different resolutions. The algorithm had a restriction on spatial dependency and it was not able to locate the objects that are smaller than a pixel. Mertens et al. (2003) advanced the work of Verhoeye and De Wulf (2002) and developed a genetic algorithm in SRM to locate sub-pixels. Though finding many parameters from the algorithm was a major advantage of the approach, results showed a higher accuracy than a traditional, hard classification.

In most of those algorithms accuracy of SRM depends upon the accuracy of classification method and spatial dependency between pixels was used only after finding fraction of each class (Kasetkasem et al., 2005).

2.4. Super resolution mapping and Markov random field

The ability of MRF models to account for the spatial dependence between the classes proportions of the neighboring pixels, in an accurate way, has been used to refine the results from a sub pixel classification (Li, 2009). Kasetkasem et al. (2005) used Markov random field based approach to generate super resolution land cover maps using IKONOS MSS and Landsat ETM+ images. The study shows that MRF models are well suited to represent the spatial dependence within and between neighboring pixels. They concluded that accuracy of land cover mapping is significantly improved by this method.

Neher and Srivastava (2005) used the Bayesian MRF framework to label the terrain using hyperspectral images. They stated that hyperspectral images point to non-Gaussian statistics of pixels values and proposed a probability model that captures non-Gaussian statistics of hyperspectral images, and used them in automated classification of terrain sites. There result demonstrated an improvement in labelling performance over the more conventional multivariate Gaussian model. Tso and Olsen (2005) improved contextual information based on MRF and multi-scale fuzzy line process for classification of IKONOS panchromatic and multi-spectral images. Their results presented success in generating the patch-wise classification patterns with increased accuracy

Hailu (2006), studied the suitability of Markov Random Field for land cover mapping. The neighborhood size was modified with respect to the scale factor and the other modification was on the Gibbs potential parameter estimations (Kasetkasem et al., 2005). The study concluded that with appropriate parameters settings, reasonable accuracy results can be attained even for classes with low separability. This makes it a highly potential method for the land cover mapping.

Tolpekin and Stein (2009) studied the effect of class separability on the accuracy of SRM. Their study introduced smoothness parameter to control the balance between likelihood and prior in the posterior energy function. It was reported that the optimal value of smoothness parameter depends on class separability and scale factor. They concluded that SRM with optimal smoothness parameter produces more accurate estimates of class area proportion as compared to those obtained with linear spectral unmixing.

Ardila et al. (2011) proposed a contextual and probabilistic method for detection of tree crowns in urban areas using a MRF based SRM approach in very high resolution images. They achieved acceptable result for detecting tree crowns in residential area of the Netherlands and they revealed that the method outperforms tree crown identification results obtained with maximum likelihood, support vector machines and SRM approaches.

Poudyal (2013) explored the possibilities of MRF based SRM for identification of row crop structure for a potato field from VHR satellite image. Findings from the study proved that SRM with high emphasis on

spatial contextual information from prior model and spectral information from imagery is able to detect row structure prominently even for relatively complex scenes with high mixed pixels and that higher accuracy can be achieved in row detection with an anisotropic prior window and with a slower simulated annealing.

3. STUDY AREA AND DATA PREPARATION

This chapter presents a brief description of the study area, field measurement, remote sensing data and their pre-processing. Section 3.1 describes the study area, while 3.2 and 3.3 describes the field data measurements and the UAV mapping system, respectively. All data used in this research are provided by the laboratory of Geo-information science and Remote Sensing Wageningen University, the Netherlands.

3.1. Study area

The study area is an agricultural parcel of potato crop located 51° 19' 04.55" N and 5° 10' 11.29" E close to the village of Reusel in the province of Noord-Brabant, in the southern Netherlands. In the field, plots of 30 by 30m were prepared and supplied with four levels (0, 25, 45 and 70 kg h-1) of Nitrogen (N) fertilization including three replicates. Figure 1 presents an overview of the experimental plots with four levels of N fertilization.

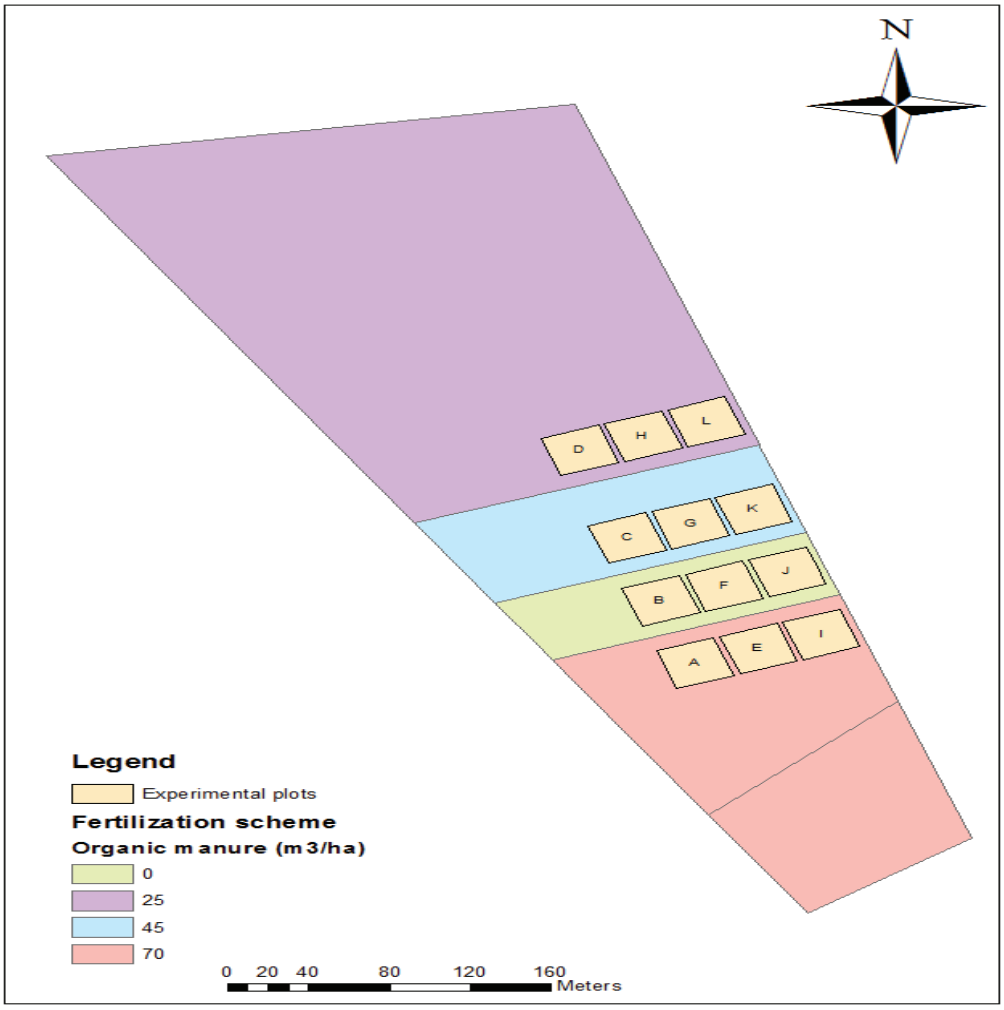

Figure 3.1: Overview of the experimental field.

3.2. Field Data

Crop parameters were measured on selected rows in the 12 experimental plots. For these measurements, each plot was divided into two; one left and one right from the tractor path and four rows per plot (i.e. two rows on each side) were selected. The crop parameters that were measured over the growing season were leaf chlorophyll content and leaf area index (LAI). The handheld Minolta SPAD-502 chlorophyll meter was used to measure the chlorophyll status per row for all plots (24 measurements per plot). In each plot, four rows were measured (rows 3 and 10 left and right to driving path) and for every row, six plants (Figure 3.2) and for every plant three leaves to characterize variability within the plots. Each reading per plant was the average result of the three-leaf chlorophyll readings (18 readings per row). The plant canopy analyser (LAI- 2000) was used to measure LAI same rows in the experimental plots. Each SPAD measurement per plant was used as input into data analysis. The shapefiles of the plots and blocks (representing each treatment levels) which have been provided in geographic lat/long coordinate system were made available for this study.

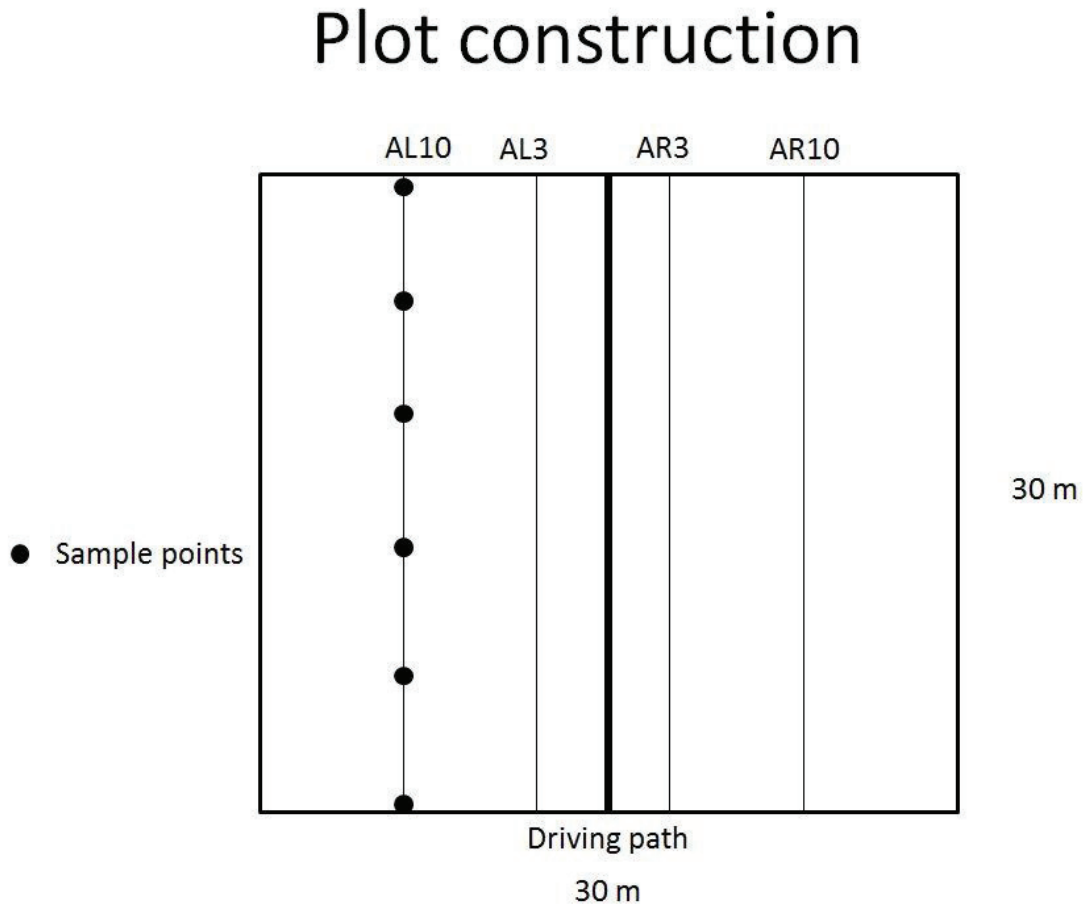

Figure 3.2: Plot construction indicating points of field measurements

A Cropscan Multispectral radiometer (MSR16R), i.e. a 16-band radiometer measuring simultaneously the reflected and incoming radiation in 16 narrow spectral bands (10nm) was used to obtain the spectral reflectance of potato

canopy. Reflectance is measured by means of a 28 field-of-view (FOV) aperture and incoming radiation using a cosine-corrected sphere. Calibration is performed by pointing the 28 FOV apertures towards the sun using an opal glass. Using this calibration, spectral reflectance is derived. Table A 3.1 shows the specification of the instrument as described in (Clevers and Kooistra, 2012) . In each plot, the same four rows were selected and six measurements per row were made.

3.3. UAV mapping system

Imaging data were collected with multispectral and hyperspectral sensors fitted to an Octocopter UAV system (Aerialtronics Altura AT8) which can carry payload up to 2kg. A detailed description on payload, camera geometric calibration, image radiometric calibration and processing chain developed for the mapping system is provided in (Suomalainen et al., 2013). The mapping system was used to acquire imagery over the experimental field for four days over the growing season: June 6, June 14, July 5 and July 17, 2013. For every day, two flights were made, one covering the six southern plots of the experiment and one covering the upper six plots of the experiment (Figure3.1). For this research, an RGB Orthophoto (1m and 0.025m spatial resolutions) and a hyperspectral image (1m spatial resolution, a spectral range of 450-950nm at 5nm band width containing 101 bands) both acquired on the 5th of July are used. The 0.025m RGB Orthophoto in this thesis is henceforth referred to as the Very High Resolution (VHR) image. Subsets from the images are shown in Figure 3.3.

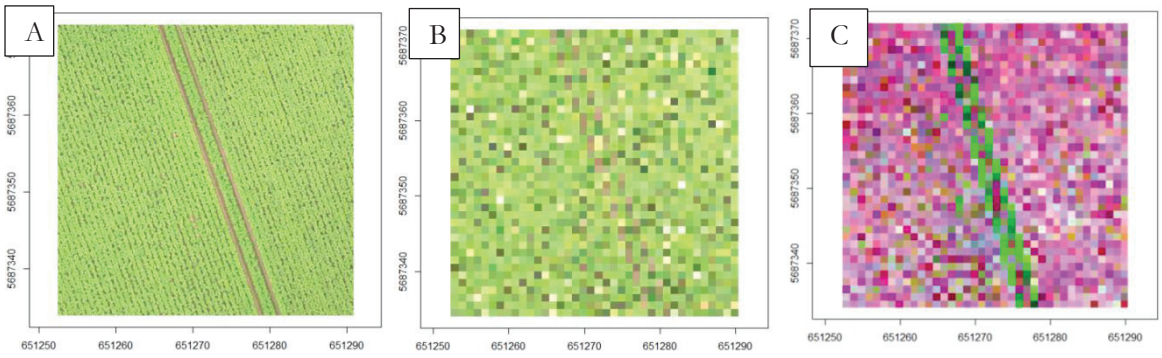

Figure 3.3: Subsets of (a) VHR image; (b) 1m Orthophoto; (c) 1m hyperspectral image of a plot in the field.

3.4. Data pre-processing

All images are provided in UTM zone 31 north spheroids and WGS 1984 datum thus, no referencing is required. Since the images are acquired using different sensors, the registration or co-registration between these images is crucial to this study. Registration is the process of geometrically aligning two or more sets of images. Firstly, to ensure conformity between the vector files and the images, the vector files were projected from geographic lat/long coordinate system to UTM zone 31N with WGS84 spheroid and datum system.

3.4.1. Co-registration of Hyperspectral image

All images are provided in UTM zone 31N spheroid and WGS 1984 datum, thus, no referencing was done. Since the two orthoimage of different resolutions (Figure 3.3) are produced from the same data source as described in (Suomalainen et al., 2013), they perfectly align together. A substantial shift of 4 m and rotation of 3º were observed between the hypercube and the orthoimages. To correct for this, resampling was not considered to be the proper choice since it involves spectral averaging that yield pixels with possible loss of information which may have adverse effect on the methodology in this study.

Subsets were made from all images corresponding to blocks (containing three plots) as described in Section 3.2. Taking the VHR image as the base, tractor paths in each of the plots visible in both the hypercube and orthophoto were digitized. The coordinates of the hypercube pixels was rotated through an angle of 3º formed by the intersection of these lines. Out of the three plots in the block, plot H was found to have a perfect alignment with the orthomosaic (Figure 3.4), whereas plots D and L have a deviation of 0.75 and 0.8 m. respectively.

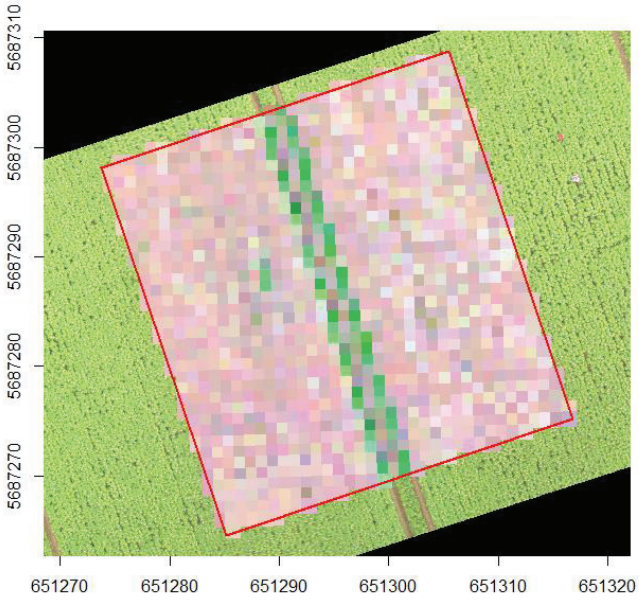

Figure 3.4: Hyperspectral image of plot H align on the VRH image after co-registration.

3.5. Software

In this study, different softwares were used for applying the proposed methodology. Envi 5.0 was used for extracting training sets from the VHR image. Erdas imagine 2013 was used to digitize tractor paths used in co-registration. All the major implementations of the techniques discussed were carried out using the R

programming language and environment for statistical computing version 3.0.2 software. R is open-source software which can be used for the statistical computing and visualization.

4. METHODOLOGY

This chapter gives an overview of the method used in achieving the stated objectives. In each section, the concepts are explained followed by its application to this study. The general methodology of this research is divided into two steps. The first step (Figure 4.1) depicts the Super resolution image restoration (SRIR) technique to produce reflectance image of canopy. The second step (Figure 4.2) investigates relationships between hyperspectral vegetation indices computed from the reflectance image obtained from MRF based SRIR and field measurement from Crop scan.

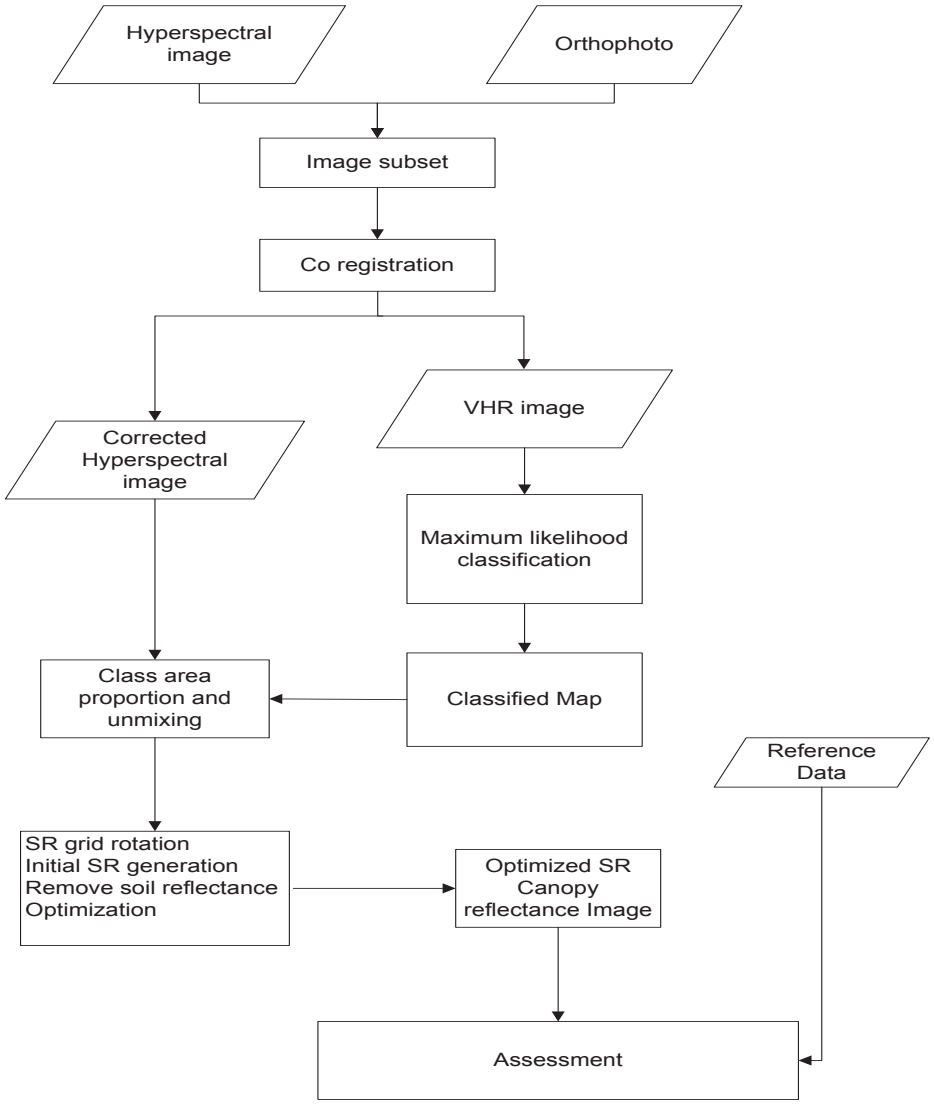

Figure 4.1: Schematic representation of MRF based SRIR for producing reflectance canopy image.

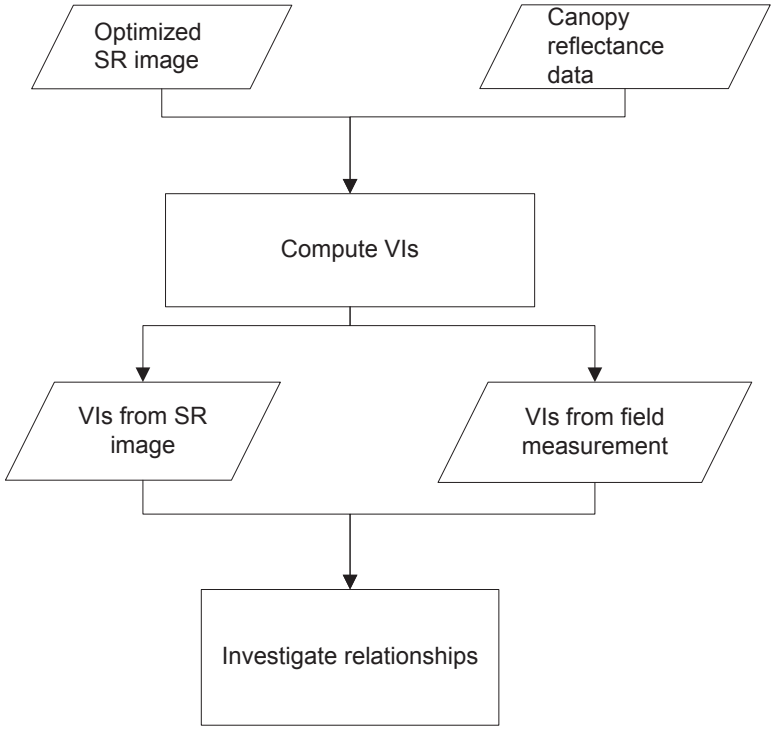

Figure 4.2: Workflow of investigating relationship between VIs derived from super resolution image and field measurement.

4.1. Class area proportions and Spectral unmixing

Hyperspectral images have high spectral information which increases the capability to detect and differentiate various land cover classes; however, the existence of mixed pixels at any spatial resolution poses a major challenge when using the conventional hard classification technique. Linear spectral unmixing is a technique designed to address the problem of mixed pixels making it possible to classify features smaller than a pixel. The linear mixture model (LMM) assumes that the signal received at the sensor is a linear combination of proportion of individual surface components present in a particular pixel (Zhu, 2005). Mathematically, the LMM is defined as:

$$X_{bi} = \sum_{k=1}^{q} \theta_{ik} m_{bk} + e_i \qquad (7)$$

Where: θ_{ik} = proportion of class *k* in pixel *i*

m_{bk} = reflectance of class *k* in band *b*

e_i = error term for band *b*

X_{bi} = measured reflectance of at spectral band *b*

q = the number of classes

The sum of all class proportions for every pixel should be equal to 1, so:

$$\sum_{k=1}^{q} \theta_{ik} = 1 \qquad \forall\, i = 1, \ldots\ldots, n$$

To derive proportion of individual classes, the procedure for unmixing generally involves three stages; dimension reduction, endmember determination and inversion of the LMM (Keshava, 2003).

Considering the resolution of the hyperspectral image (1 m) used in this study, applying standard training procedure (i.e. finding pure pixels) is not possible owing to the absence of pure pixels. It is a common approach to use a fine spatial resolution image to estimate the class area proportion (Adams and Gillespie, 2006). In addition, if classes are highly separable, the use of likelihood functions as estimators of mixing is valid (Schowengerdt, 1996).

In this study, maximum likelihood classification (MLC) result of the VHR image was used for training the hyperspectral image since the two images have been spatially registered (see Section 3.4.1). By identifying the overlapping pixels, the proportions of the components in the hyperspectral image are computed. The LMM is then modified to estimate the mean spectral reflectance of the components *(canopy* and *soil)* in the hyperspectral image. Based on the assumption of LMM, for every pixel in all spectral bands, a set of linear equations (7) is established and solved by singular value decomposition technique (SVD).

4.2. MRF based super resolution image restoration

The purpose of this method is to predict the reflectance of canopy from the observed coarse resolution hyperspectral image at a higher resolution.

4.2.1. Mathematical concepts of Super resolution

Let y be a coarse resolution hyperspectral image that contains K spectral bands. The pixel locations are denoted as $b_i \in B$ where B is pixels matrix with size $M \times N$. The spatial resolution of the image is denoted by R hence every pixel b_i is assumed to correspond with a square area on the ground of size R^2.

Result of super resolution is an image x at a finer spatial resolution r such that $r < R$. The pixel locations are denoted as $a_j \in A$ where A is a set of pixels with size $M_f \times N_f$. The relationship between x and y can be expressed schematically in Figure 4.1.

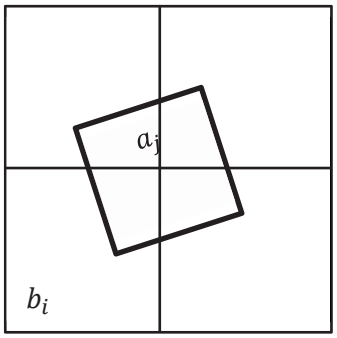

Figure 4.3: Footprints of pixels a_j and b_i showing relationship between fine and coarse resolution images

In this study, the relationship between the super resolution image x and coarse resolution image y is modelled as:

$$y(b_i) = \sum_{a_j \cap b_i} x(a_j)\, \psi_{ji} \tag{8}$$

Where $a_j \cap b_i \neq \emptyset$

The expression ψ_{ji} is chosen as weight such that:

$$\psi_{ji} = \frac{A(a_j \cap b_i)}{A(a_j)} \tag{9}$$

4.2.2. Setting up the super resolution grid

Based on preliminary knowledge of the field structure (i.e. distance between rows is 75 cm) the cell size of the output super resolution (SR) image was defined as 0.75 × 0.75 m. The grid of the SR image was rotated with respect to the grid of the coarse input image by 3° to align with row direction (see Figure 3.3a for row orientation) in the field.

The link between the pixels of the SR grid and input image pixels were established using geographic coordinates. To achieve this, spatial polygon footprints of the coarse image was used such that centres of SR image pixels fall inside the footprints. The output of the initial SR image x contains isolated pixels which should be optimised considering spatial dependence.

4.3. MRF and Gibbs random field

This section provides the theoretical background of Markov random field; it's equivalence with Gibbs and implementation in this current study.

Consider a set of random variables $d = \{d_1, d_2, \ldots, d_n\}$ defined on the set K where $d \in L(1 \leq i \leq n)$ are set of pixels DN values. The family d is called a random field.

To model image x as a MRF, it must satisfy the following properties:

- Positivity: $P(x) > 0$, when this condition is satisfied, the joint probability $P(x)$ of any random field is uniquely determined by its local conditional probabilities.
- Markovianity: $P(x_i|x_{K-i}) = P(x_i|x_{N_i})$ i.e. the labelling of the central pixel is only dependent on its neighboring pixels. In the context of classification it implies that same land cover class is more likely to occur in nearest region than isolated pixels.
- Homogeneity: $P(x_i|x_{N_i})$ is same for all sites i

Where; $K - i$ represent all pixels in the set K excluding the central pixel i and N_i denotes the neighbour of pixel i.

The posterior probability for pixels of image x given the observed image y can be specified by means of a posterior energy function:

$$P(x|y) = \frac{1}{Z}\exp\left(-\frac{U(x|y)}{T}\right) \quad (10)$$

Where Z is normalizing constant and T is a constant termed temperature, $U(x|y)$ is the posterior energy function of image x given the observed image y. We can say that maximizing $P(x|y)$ is equivalent to minimizing the energy function which can be formulated as:

$$U(x) = \sum_{c \in C} V_c\,(c) \quad (11)$$

Where $V_c(c)$ is the potential function regarding clique C. A clique is a subset of a neighbourhood system, where all pairs of site are mutual neighbours. It can be single site, pair of sites or triple of neighbouring sites. In this study pair-wise clique was used.

Prior Energy

Assuming image x has MRF properties, the prior energy is modelled as sum of pair-site interaction as follows:

$$U(x) = \frac{1}{2}\sum_{j=1}^{N}\sum_{l \epsilon N(a_j)} \omega(a_l)\,\delta\left(x(a_j), x(a_l)\right) \quad (12)$$

Here, $U(x(a_i))$ is the local contribution of prior energy from pixel $x(a_j)$, $U(x)$ is the prior energy function of image x, $N(a_j)$ is the neighbourhood system, $\omega(a_l)$ denotes the contributing weight from

pixel $a_l \epsilon N(a_j)$ to prior energy and $\delta(\alpha, \beta)$ is the interaction between neighbouring pixels such that $(\alpha - \beta)^2$ is small for similar pixels and otherwise for dissimilar pixels. The weight $\omega(a_l)$ is modelled as:

$$\omega(a_l) = \begin{Bmatrix} \Phi(a_l), & central\ column \\ w_m \Phi(a_l), & otherwise \end{Bmatrix} \tag{13}$$

The parameter w_m $(0 \leq w_m < \infty)$ is the weight multiplier and it controls the overall magnitude of the weights. $\Phi(a_l)$ is utilised as an anisotropic expression that depends only on distance $d(a_j, a_l)$ between pixels a_j and a_l. It is given by:

$$\Phi(a_l) = \frac{\zeta}{d(a_j, a_l)} \tag{14}$$

ζ is a normalisation constant chosen such that $\sum_{l \epsilon N} \Phi(a_l) = 1$ for non-boundary pixels

The complete neighbourhood is defined as a set of all pixels inside a rectangular window (Figure 4.1) excluding the center pixel a_j with window sizes $2W_x + 1$ and $2W_y + 1$ being the length of the rectangular sides.

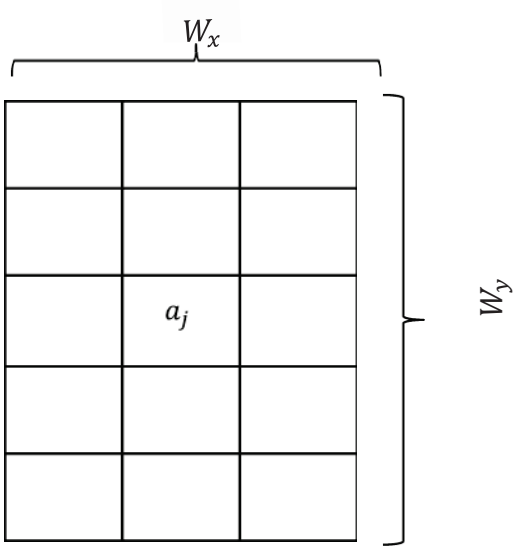

Figure 4.4: Neighbourhood system of pixel used in this study

To predict the pixel value a_j that corresponds to minimum energy solution, different neighbourhood window sizes were tested. The number of maximum neighbourhood system is given by:

$$N_{max} = (2 \times W_y + 1) \times (2 \times W_x + 1) - 1 \tag{15}$$

Where W_y and W_x are window sizes along the row and across the row of pixel a_j respectively. To ensure prominent row structure in the image, anisotropic property of MRF was considered for assigning weight

to pixels in the neighbourhood. Throughout this study, W_x is fixed at a value 1 corresponding to window size 1 to limit the number of neighbouring pixels across the row to be considered during predicting of pixel value.

Conditional energy function

Based on the relation defined in Equation 8, we define the conditional energy function of image y given image x as:

$$U\left(y(b_i)\middle|x(a_j)\right) = \varphi_{ij}\sum_{k=1}^{N_b}\left(y(b_i) - \sum_{a_m \cap b_i \neq \emptyset} x_k\,(a_m)\psi_{im}\right)^2 \quad (16)$$

Where: $\boldsymbol{\varphi_{ij}} = \frac{\boldsymbol{A(a_j \cap b_i)}}{\boldsymbol{A(a_j)}}$

Posterior Energy

By combining equation 12 and 16, the global energy U_{global} can be defined by:

$$U_{global} = \lambda U_{prior} + (1-\lambda)U_{likelihood} \quad (17)$$

The smoothness parameter λ controls the contributions from the likelihood and prior models. It takes value between 0 and 1. If λ is set to 1, it implies the likelihood model is completely ignored and minimum posterior energy is obtained for images where all pixels are assigned same value.

Prediction of pixel values in image x is performed by minimizing this energy function to get the optimal solution maximum a posteriori (MAP):

$$\hat{x} = \arg\, min\{\lambda U(x) + (1-\lambda)U(x|y)\} \quad (16)$$

The solution of the above equation requires specially designed approach. Normally, an iterative approach is used because the estimation of each pixel has an effect on those assigned to its neighbours (Li, 2009). In order to solve the equation, simulated annealing (SA) algorithm was adopted. It is brief explained in the Section 4.4.

4.4. Simulated annealing algorithm

Simulated annealing (SA) is a stochastic iterative algorithm for global optimization problem. It includes the annealing parameters (i.e. initial temperature T_0 and updating temperature T_{upd}) which control the process. The algorithm starts at high temperature and slowly cools down to an ordered stage based on a

carefully defined cooling schedule. In this study the cooling schedule is expressed by $T = T_0 \times T_{upd}$ T is the next temperature value depending on the next iteration. The process is repeated until the system becomes frozen (i.e. T→0), implying that pixels stop updating. High temperature refers to the state when large number of pixels has different values showing high randomness which increases probability of a pixel being replaced by new value. As the optimization continues, the algorithm tries to find the global minimum.

4.5. Accuracy asssessment

Accuracy assessment is done by evaluating the result against the reference data which was generated from the VHR image. In this context, accuracy refers to the level of agreement between the result and the reference data. In other words, how far the super resolution image is able to capture prominent features e.g. tractor driving path and missing plants in the field.

Error matrix from which accuracy measures such as producer accuracy, user accuracy and overall accuracy was derived. Producer accuracy is a measure of omission error and is obtained by dividing number of correctly classified pixels in each class by the total number of pixels in that class. User accuracy is a measure of commission error. It denotes the probability that a pixel labelled as a certain cover class in the image really belongs to that class. The overall accuracy is the number of correctly classified pixels divided by the total number of pixels checked.

To validate the super resolution image, prominent features in the field e.g. tractor driving paths and missing plants were identified in the VRH image and compared to result from the super resolution analysis using this accuracy measures described above.

Experiments to determine optimal MRF parameter values were performed by determining their correspondence with the accuracy measures. The reproducibility of the result was evaluated by performing 10 experiments for each parameter and computing the mean accuracy, energy and iteration.

The predicted reflectance from the optimised super resolution result was compared to canopy reflectance measure from the field. For this comparison, average values of canopy reflectance of rows measured in the field were used.

4.6. Relatioship between HVIs derived from field measurement and SR image

The vegetation indices highlighted in Table 2.1 were calculated from the SR image and field data. To investigate relationship between these indices, average value of four rows from which measurement were made in the field were computed from the SR image. These indices were further analysed in linear regression model to identify any possible relationship.

5. RESULTS

5.1. Class area proportion estimation

Two classes were considered in this study *(canopy* and *soil)*. Figure 5.1 show the estimated mean reflectance from unmixing compared to reflectance measurement in the field.

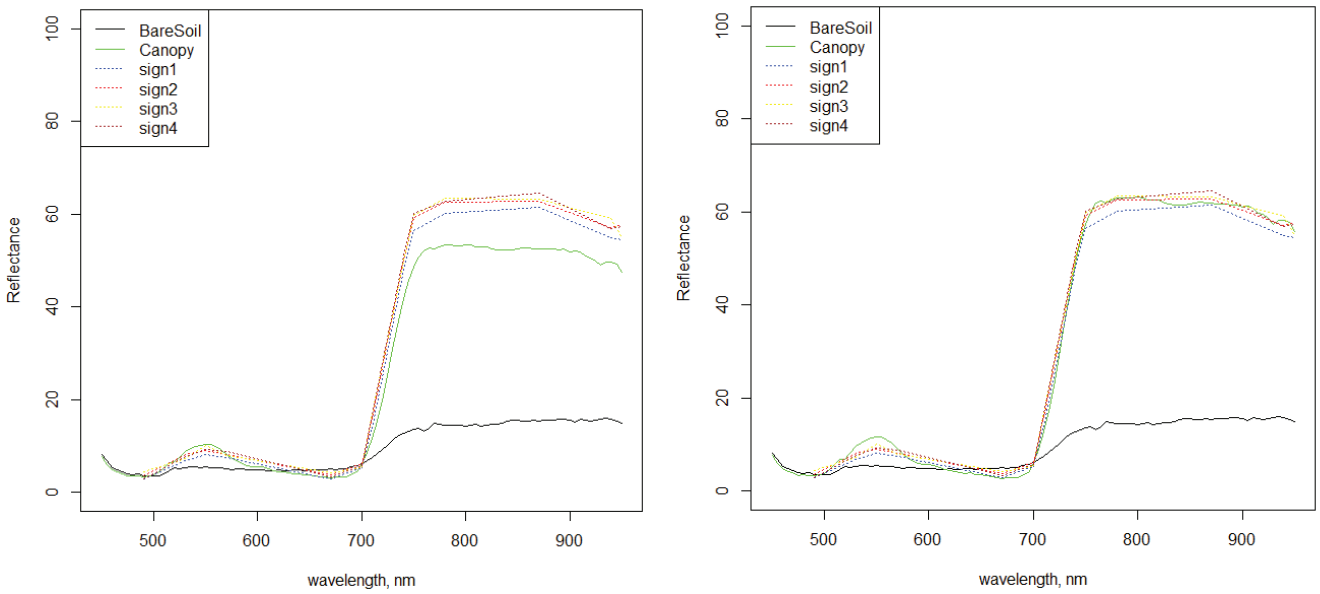

(a) (b)

Figure 5.1: Mean reflectance of canopy derived from hyperspectral image before (a) and after correction (b) to field measurement. Sign 1-4 represent mean Canopy reflectance measured from four rows in the field.

From Figure 5.1(a), it can be observed that there is bias in the estimation of mean canopy reflectance which may be attributed to the procedure of maximum likelihood classification of the VHR image or overlap between canopy and interlocking of plants between the rows. Based on this observation, correction was applied by reducing proportion of canopy by 0.8 in the image. Figure 5.2 shows the agreement between the mean canopy reflectance and the field data.

5.2. Experimental results from MRF based super resolution image restoration

As explained in Section 4.3, assigning pixel values in the initial SR image was performed randomly therefore, it is expected to have many isolated pixels and optimisation is required. For the optimisation process, it is essential that appropriate value of MRF parameters is used. These parameters include neighborhood size (W_y), smoothing parameter (λ), weight multiplier (w_m) and annealing parameters (T_0 and T_{upd}). Therefore, several experiments were performed in search of optimal parameter values and the

quality of the results in terms of achieving minimum energy solution for predicting canopy reflectance in the plot were evaluated using accuracy measures described in Section 4.5. For each investigated parameter, 10 repetitive experiments were performed for same settings. We compute the mean and standard deviation of energy and accuracy values to evaluate the reproducibility of result. In the following subsections we present result of experiments performed and observations made from the result.

5.3. Initial temperature

The aim of this experiment is to identify the optimal initial temperature T_0 that corresponds to minimum energy solution. Each experiment was repeated for 10 times for T_0 values of 0.01, 0.1, 0, 1, 2, 3, 4 and 10 for fixed values of other parameters ($W_m = 0, T_0 = 3,\ \lambda = 0.7, W_{size} = 5$ and $T_{upd} = 0.9$). The summary of the result for this experiment showing the mean minimum energy and standard deviation is presented in Figure 5.2. For the purpose of display, only the results of T_0 values in the range between 0.01 and 10 are shown.

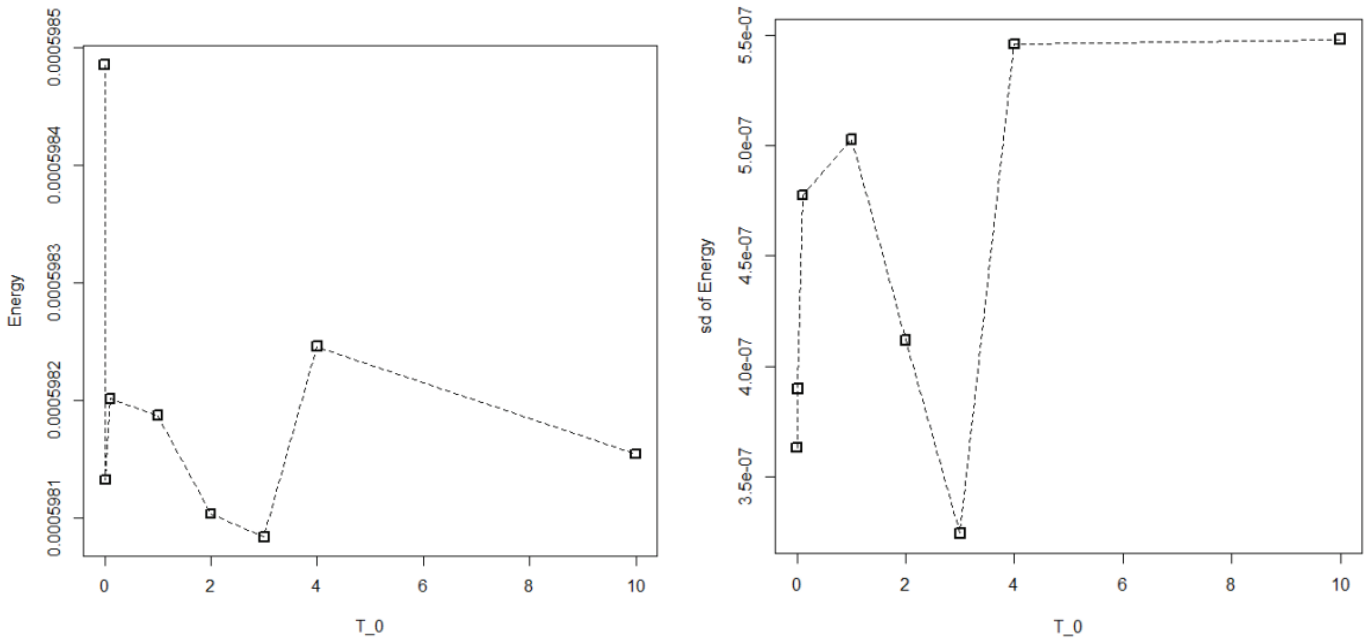

Figure 5.2: Mean minimum energy and standard deviation for different T_0 values

From Figure 5.2 (a), it can be observed that values close to $T_0 = 0$ give higher energies and there is a clear minimum at $T_0 = 3$. The standard deviation presented in Figure 5.2 (b) shows the variation of the minimum energy found at different values of initial temperatures. Again, $T_0 = 3$ have the least standard deviation. Although the minimum energy observed at $T_0 = 3$ is not much less than the rest, it is a preferred choice because it has the lowest mean and standard deviation.

5.4. Experimental results on updating schedule

In this experiment we search for a value of temperature update T_{upd} where optimum super resolution result can be achieved. Like the experiment for T_0, different values of T_{upd} (0.1, 0.5, 0.8, 0.9, 0.95, 0.97 and 0.99) were considered while other parameters are fixed with T_0 taking a value of 3 as determined from experiment in Section 5.3. Figure 5.3 shows the plot of the mean minimum energy and standard deviation achieved for 10 experiments at different values of T_{upd}.

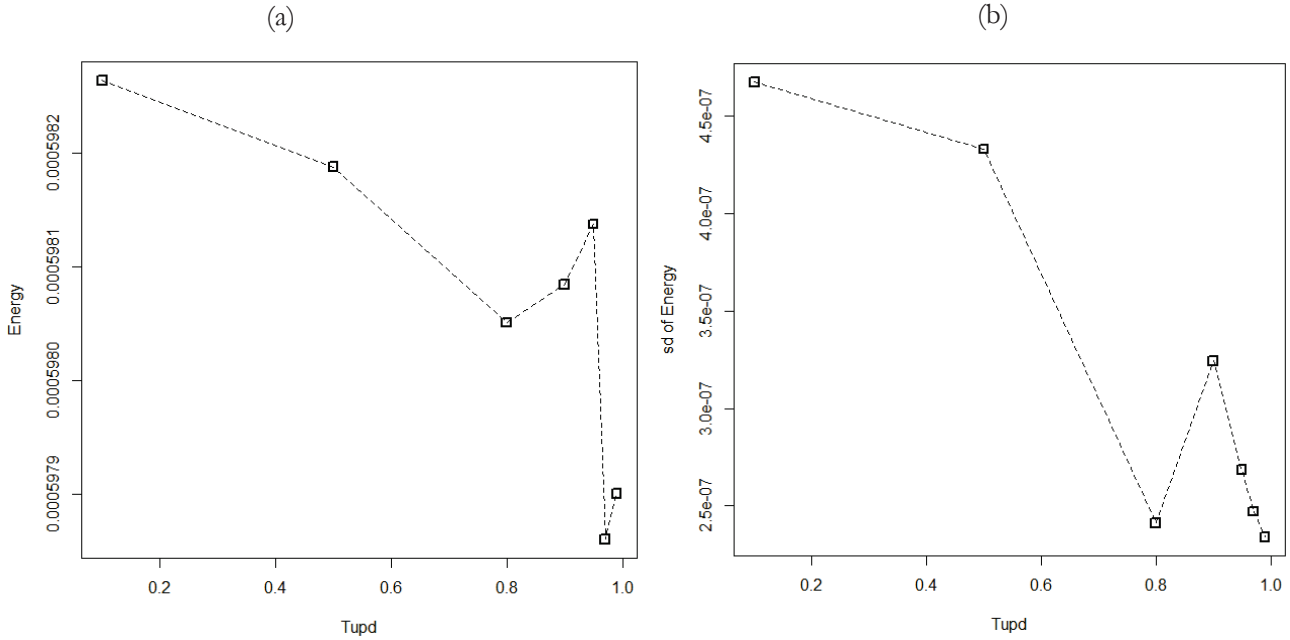

Figure 5.3: Mean minimum energy and standard deviation for different T_{upd} values

The above figure shows similar trend in minimum energy and standard deviation for all values of T_{upd} used in the experiment. $T_{upd} = 0.99$ have the least variation in energy values obtained for the 10 experiments. These energy values however, are high as compared to $T_{upd} = 0.97$. Therefore, $T_{upd} = 0.97$ is considered to be suited for implementation purpose.

5.5. Neighbourhood window size determination

As discussed in Section 4.2, two different types of windows (W_x and W_y) were used in this study to ensure prediction of pixel values and to maintain the row structure of the field in the resulting image. These two different windows combined together define the number of maximum neighbourhood system as depicted in Equation 9. This experiment aims at finding optimal W_y that corresponds to high quality result. To choose appropriate window size, quality of results from seven different windows of sizes 1, 2, 3, 4, 5, 6 and 7 were evaluated. In this experiment, the parameters were set to $\lambda = 0.7$, $T_0 = 3$, $T_{upd} = 0.97$ and $w_m = -0.25$. To evaluate the reproducibility of the result, each experiment was repeated for 10 times for same parameter settings. The optimised super resolution images for window sizes 5, 2 and 4 are shown in Figure 5.4

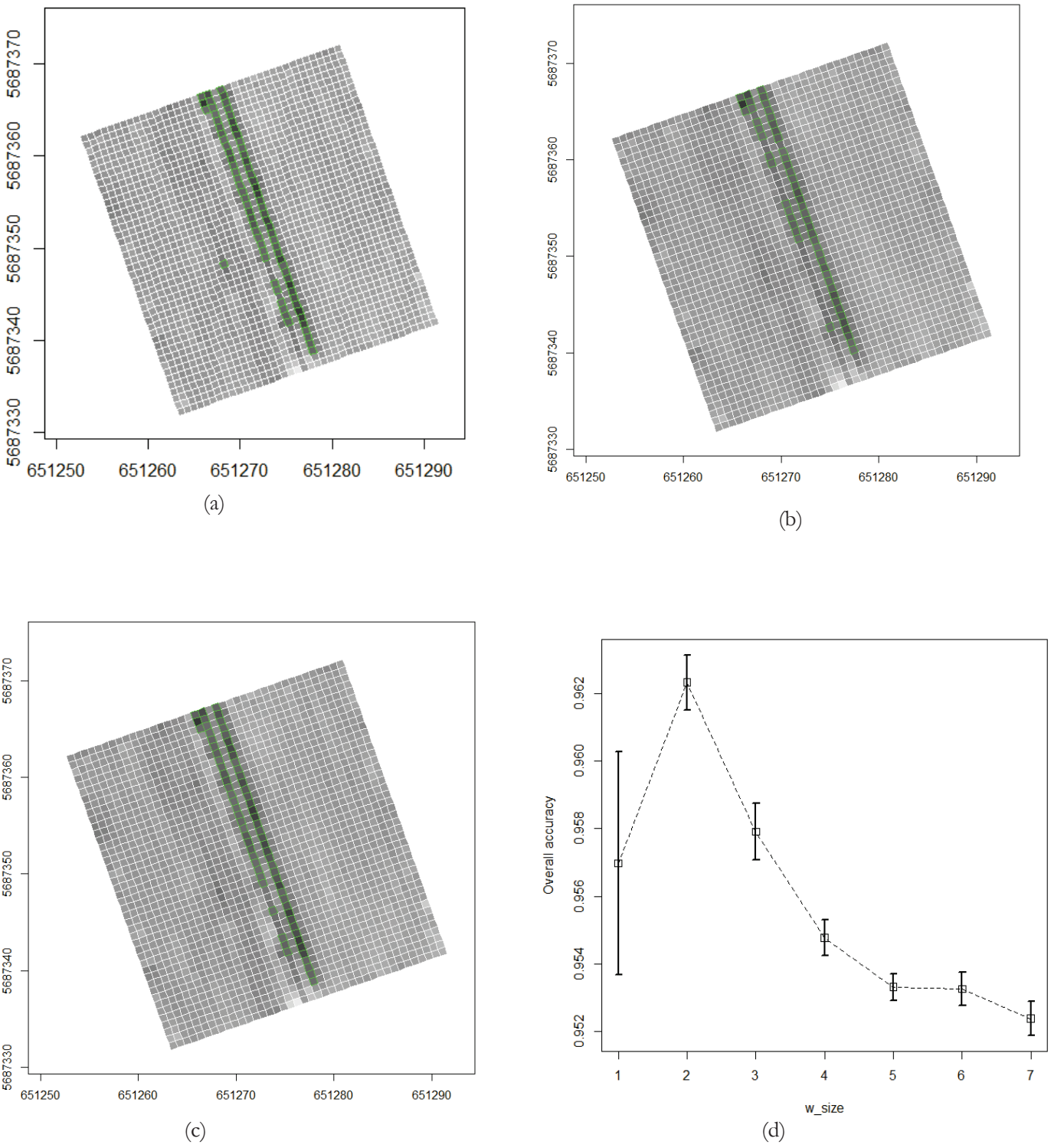

Figure 5.4: Optimised SR image for size (a)5; (b) 2 and (c) 4.The green rectangles in the images represent the tractor driving path. (d) Overall accuracy for different values of window sizes.

The accuracy gives the quality of the result while the standard deviation which is displayed using the error bar shows variation in the results. Observation from Figure 5.4d shows high OA for window size 2 however, visual inspection of the resulting image show some pixels along the driving path. Also, there is

high variation in the results obtained from the 10 repetitive experiments suggesting that results are not reproducible. On the other hand, for window size 4 show better results compared to window size 2. For window size 5, visual inspection of resulting images from the 10 experiments show comparable results, this is also confirmed by the minimum deviation from the mean OA as by the error bar in the OA plot. To aid the choice of appropriate window size, we also inspect the plot of the user accuracy (UA) and producer accuracy (PA) as show in Figure 5.5.

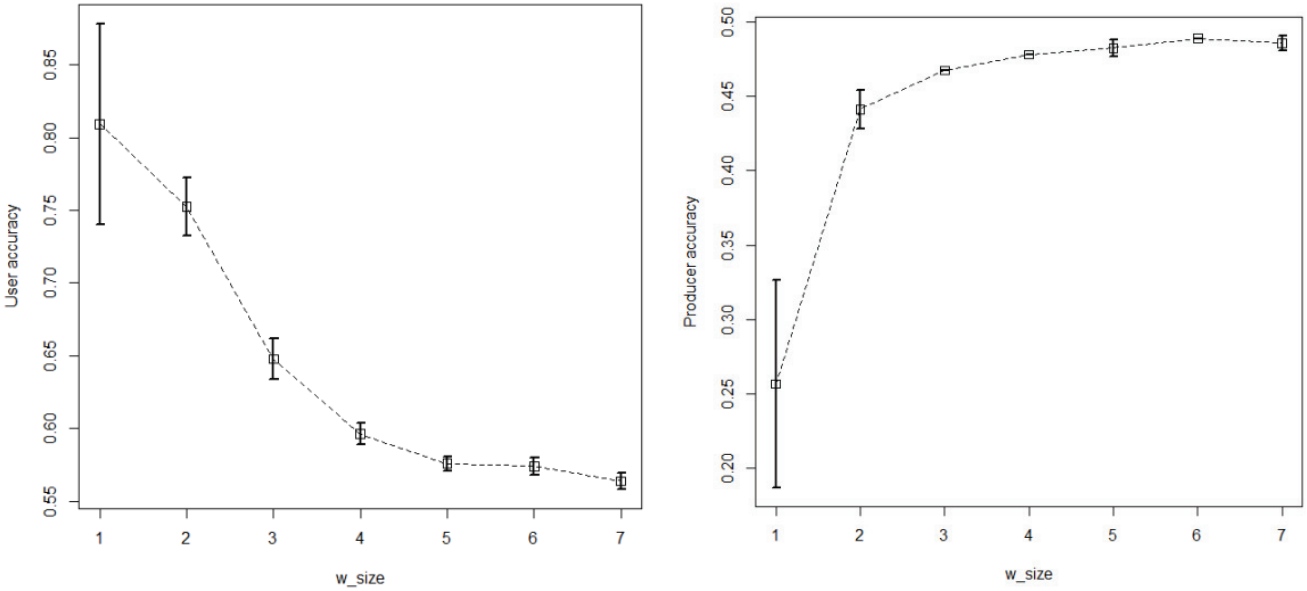

(a) (b)

Figure 5.5: User accuracy (a) and producer accuracy (b) for different values of window sizes

In Figure 5.5a, we observe decreasing trend in deviation from the mean UA for the entire window sizes with window size 5 having the minimum. The deviation from mean PA observed in Figure 5.5b for window size 5 can be compared to those observed from OA and UA, this could be another indication of high quality result. Base on the observations made so far from the optimised image and the accuracy plots, window size of 5 is chosen as appropriate.

5.6. Experimental result on weight multiplier

This parameter w_m is introduced in this study to control the overall magnitude of contributing weight from each neighbouring pixels to prior energy (see Section 4.4). The weight given to each neighbouring pixel is computed using Equation (13). Considering the importance of this parameter to the prior, it is therefore necessary to investigate its optimal value corresponding to high quality result. For this experiment, a wider range of values from -0.5 to 0.5 was investigated. Results are presented in the Figure 5.6.

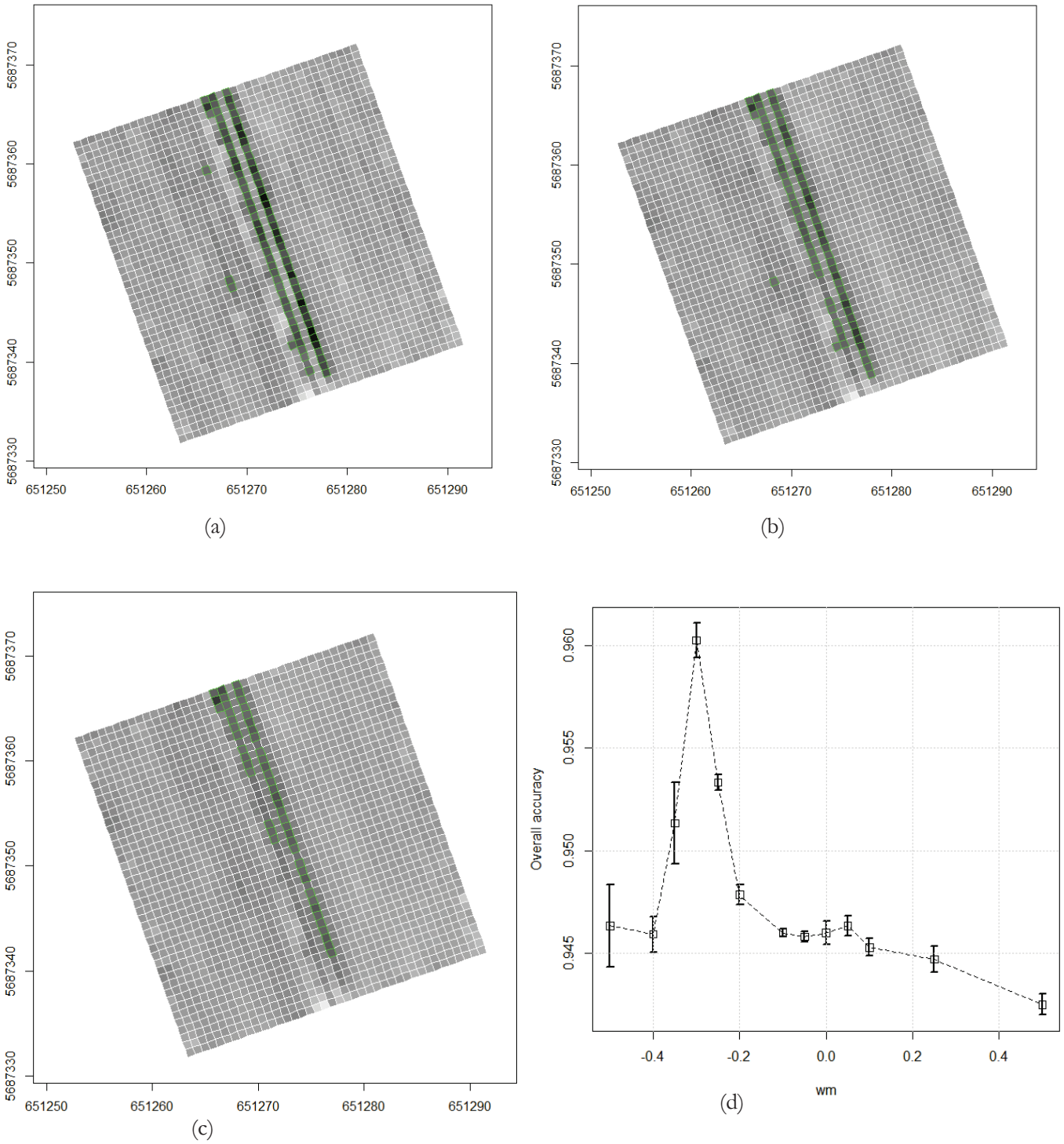

Figure 5.6: Optimised SR image for weight multiplier w_m (a) -0.25; (b) -0.2 and (c) -0.3 showing tractor driving path and missing plant along the row; (d) summary overall accuracy for different values of weight multiplier for 10 experiments.

From the accuracy plot, we notice that the maximum OA is achieved for $w_m = -0.3$ but that the optimized image (Figure 5.5c) did not capture the missing plant and driving path compare to $w_m = -0.25$ with close OA. This further confirms variation in the result as depicted by the error bar in OA plot. For $w_m - 0.2\ and - 0.25$, results are similar but base on visual inspection $w_m - 0.25$ tends to be smooth, hence this value is selected in this study.

5.7. Optimal smoothness parameter estimation

The smoothness parameter λ controls the relation between the values prior and likelihood energy (see equation 15). This experiment was performed for several values of λ (0, 0.1, 0.2, 0.3, 0.4, 0.5, 0.6, 0.65, 0.7, 0.75, 0.8, 0.85, 0.9, 0.95 and 0.99) with initial temperature $T_0 = 3$, $T_{upd} = 0.97$, $w_m = -0.25$ and $w_y = 5$.

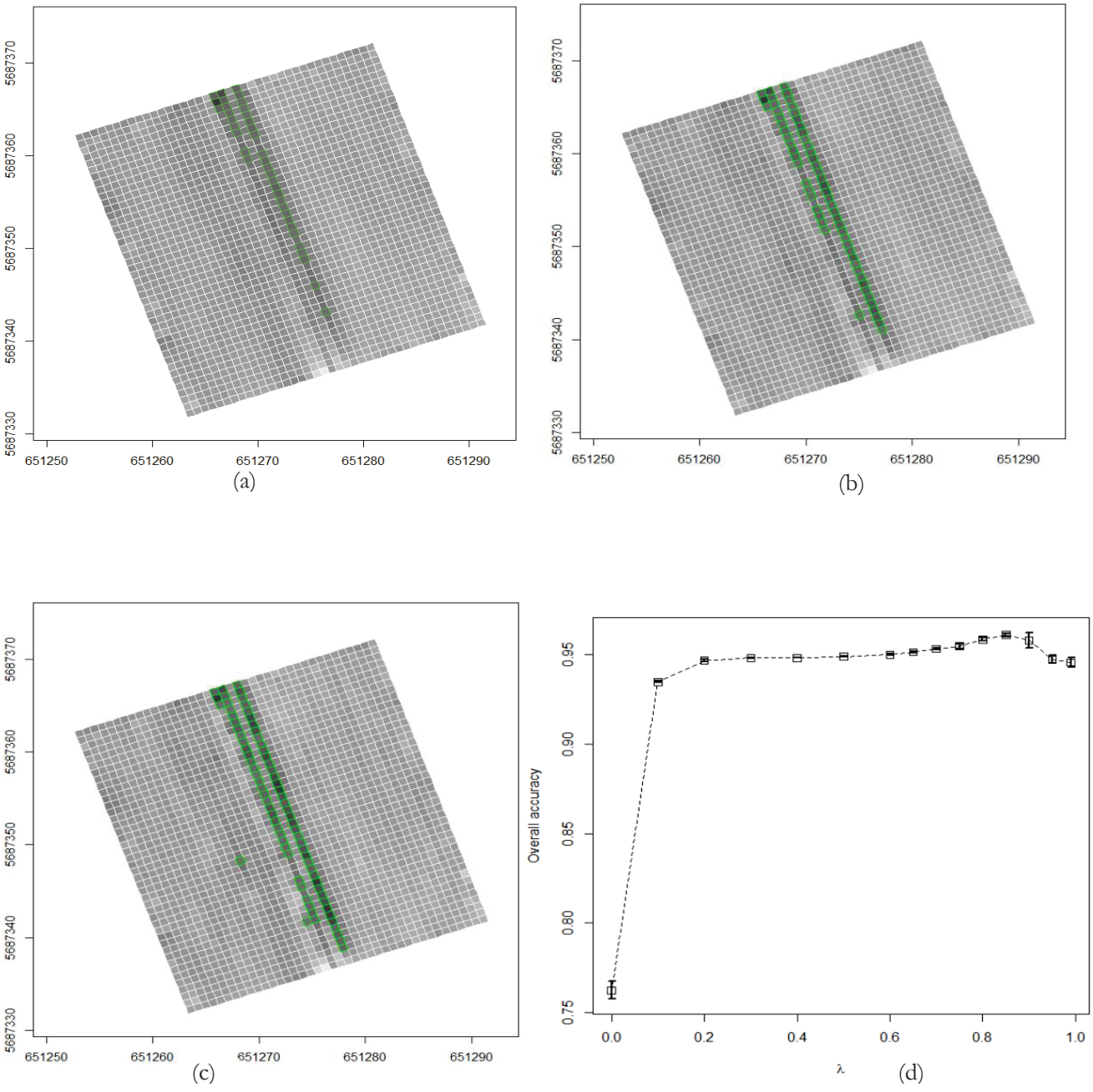

Figure 5.7: Optimised SR image for smoothness parameter λ (a) 0.90; (b) 0.8 and (c) 0.7 showing tractor driving path and missing plant along the row; (d) summary overall accuracy for different values of λ for 10 experiments

Observation from Figure 5.7d shows that the optimal value for high quality SR result is within the range from 0.6 to 0.8. As we move close to 1 over smoothing occurs in the result indicating that the likelihood is ignored (see equation 16) and only the prior is considered in predicting the pixel values of the image. The observation is confirmed by Figure 5.6b and 5.6d. For this reason 0.7 was chosen to be optimal value for the smoothness parameter. This experiment concludes the optimisation of SRM parameters.

5.8. Validating predicted reflectance from super resolution result.

After optimisation of all parameters, the predicted reflectance values of canopy from the optimized SR image were extracted along the rows from which field measurement was taken (Section 3.2). For comparison with field measurement, an average reflectance value of canopy per row was used. Figure 5.8 present the result of comparison from seven bands. These bands were selected because of they are common to both field and imagining sensors.

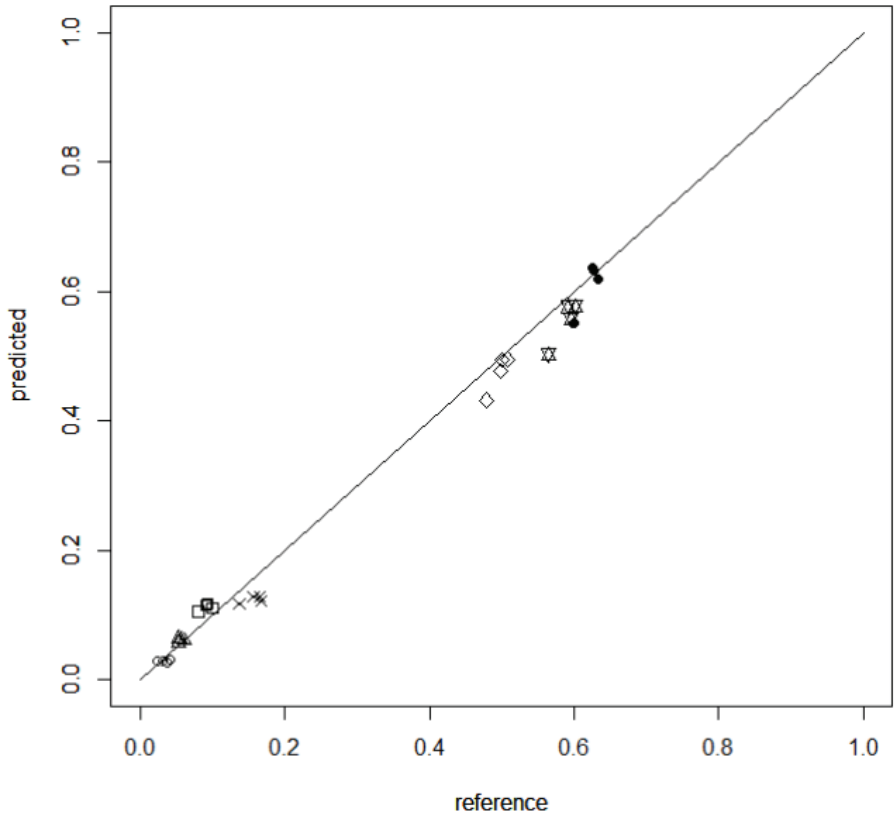

Figure 5.8: Comparison between canopy reflectance measured from the field and predicted reflectance from SR image in bands common to both sensing device.

From Figure 5.8, a strong linear relation is observed between the predicted and measured values. The root mean square of the predicted compared to the measured values is 0.04 equivalent to 4% of predicted values. This gives an indication that result is suitable for further analysis.

5.9. Relationship between hypespectral vegetation indices derived from field measurement and SR image

One of the objectives of this study is to relate in situ measurement to hyperspectral derived parameters. The relationship between VIs derived from spectral reflectance measurement of canopy from the field and SR image were investigated. The relationship between the indices is presented in Figure B.1 Appendix B. The summary result is presented in Table 5.1.

INDEX	R^2	RMSE
NDRE	0.41	0.01
REP	0.84	0.33
CL red edge	0.87	0.99
CL green	0.55	2.03
TCARI	0.72	0.07
OSAVI	0.06	0.02
TCARI/OSAVI	0.91	0.08

Table 5.1: Summary of relationship between Vegetation indices derived from SR image and in situ measurement.

From Table 5.1, high relation is expected from the indices because in the field measurement with Cropscan, the effect of soil background is minimized. Another reason why a high relation could be expected is the comparable pixel size of SR image (0.75 m^2) and Cropscan of 0.6 m^2.

6. DISCUSSION

In this study, MRF based super resolution image restoration was developed and implemented on coarse hyperspectral image of farm field to obtain a high resolution reflectance image of vegetation.

Two classes were defined and their area proportion of in the hyperspectral image was obtained by using MLC result of VHR image having obtained a match between the two images. Though not a straight forward process, the co-registration of the images was achieved geometrically to sub pixel level as explained in Section 3.4.1. Result from spectral unmixing shows a good agreement with field data as presented in Figure 5.1b. Based on result from unmixing soil contribution in the coarse image was subtracted resulting image is an image of canopy reflectance.

For the setup in this study, prior knowledge of the field was incorporated in defining the SR image grid. A thorough analysis of the intersection of pixels in the coarse and fine images was performed based on analysis of the footprint polygons (see Figure4.1). The relationship between the two images was established as in equation 8. Using the relation established in Equation 8, the conditional energy function was formulated (see Equation14). SA was employed to find the minimum energy solution that corresponds to optimal SR image.

Findings from the experimental result on initial temperature show that the resulting super resolution image is optimised at $T_0 = 3$ (see Figure 5.2a) and this result is reproducible .This experimental finding is in agreement with previous studies on MRF. Findings also reveal that with slower temperature update, the probability of pixels being replaced by new value increased. Therefore, for optimal solution, simulated annealing should be done at a slow cooling rate. The optimal T_{upd} value was found to be 0.97. Next, results on smoothness parameter indicate that larger value results in an image have same pixel values. For quality result, smoothness parameter values should be within the range 0.4 to 0.8. The optimal for λ in this study is 0.7

The relationships observed between indices computed from SR image and in situ measurement has opened up possibilities for employing MRF based super resolution image restoration technique in extracting plant information without the influence of soil background. The outcome of this study opens up opportunities for further application to different crops and different sizes of objects. It could be helpful for farmers who are limited with availability of high spatial resolution image for examining variability in crop properties.

The time required for estimating parameters is a threat to this method. Better results are possible for simulated annealing with high cooling schedule but it is computational expensive.

7. CONCLUSION AND RECOMMENDATIONS

The aim of this research is to explore the possibility of retrieving crop parameters from hyperspectral image using MRF based super resolution analysis to support precision agriculture.
It includes the following sub- objectives:

- Estimate reflectance of canopy from hyperspectral image using MRF and super resolution analysis.
- Derive hyperspectral vegetation indices (HVIs) that are sensitive to chlorophyll content as reported in literature (Clevers and Kooistra, 2012).
- Investigate relationship between HVIs derived from in situ measurement and hyperspectral image.

Four research questions were formulated in achieving these objectives. Discussion of results was done in chapter 6. This chapter aims to draw conclusion by providing answers to the research questions. Furthermore, recommendations are made for further research.

7.1. Conclusion

This sub section addresses the research questions and corresponding answers.

- Is it possible to predict canopy reflectance using MRF and super resolution analysis?

From findings in this study, it was found that for slower simulated annealing, optimal canopy reflectance image can be obtained.

- What are the optimal parameter settings to obtain the best super resolution result?

From the experiments conducted on parameters, the following values $T_0 = 3$, $T_{upd} = 0.97$, $w_m = -0.25$, $\lambda = 0.7$ and $W_{size} = 5$ were found to be optimal.

- How can the result of super resolution analysis be validated?

Validation of the SR image was done by comparing it with VHR image with accuracy measures. Predicted canopy reflectance was compared to measurement from the field.

- Is there any relationship between VIs derived from field measurement and super resolution image?

Result of comparison showed that there is a strong relationship between indices computed from the SR image and the field. This is an indication that the method implemented in deriving the reflectance image is promising.

7.2. Recommendation

Accurate retrieving of crop parameters to support precision agriculture requires discrimination of mixtures at sub pixel scales. In this study, MRF based super resolution image restoration was developed and

implemented. The method produced reflectance image of canopy at a high resolution. Result was validated with field data.

In summary there are also some other priorities to be addressed by further research:

- For energy minimisation, Simulated annealing algorithm was used this study, this algorithm is computational expensive hence other optimisation methods for instance graph cut and belief propagation (Li, 2009; Tappen and Freeman, 2003) should be investigated.
- This method could further be extended to cover different levels of Nitrogen application in the plot.

LIST OF REFERENCES

Adams, John B, & Gillespie, Alan R. (2006). *Remote sensing of landscapes with spectral images: A physical modeling approach*: Cambridge University Press.

Aplin, P., & Atkinson, P. M. (2001). Sub-pixel land cover mapping for per-field classification. *International Journal of Remote Sensing, 22*(14), 2853-2858. doi: 10.1080/01431160110053176

Ardila, J. P., Tolpekin, V. A., Bijker, W., & Stein, A. (2011). Markov-random-field-based super-resolution mapping for identification of urban trees in VHR images. *Isprs Journal of Photogrammetry and Remote Sensing, 66*(6), 762-775. doi: 10.1016/j.isprsjprs.2011.08.002

Atkinson, PeterM. (1997). Mapping sub-pixel boundaries from remotely sensed images. *Innovations in GIS, 4*, 166-180.

Bala, SK, & Islam, AS. (2009). Correlation between potato yield and MODIS-derived vegetation indices. *International Journal of Remote Sensing, 30*(10), 2491-2507.

Berni, J., Zarco-Tejada, P. J., Suarez, L., & Fereres, E. (2009). Thermal and Narrowband Multispectral Remote Sensing for Vegetation Monitoring From an Unmanned Aerial Vehicle. *Geoscience and Remote Sensing, IEEE Transactions on, 47*(3), 722-738. doi: 10.1109/TGRS.2008.2010457

Broge, N. H., & Mortensen, J. V. (2002). Deriving green crop area index and canopy chlorophyll density of winter wheat from spectral reflectance data. *Remote Sensing of Environment, 81*(1), 45-57. doi: http://dx.doi.org/10.1016/S0034-4257(01)00332-7

Cetin, H., Pafford, J. T., & Mueller, T. G. (2005, 9-11 June 2005). *Precision agriculture using hyperspectral remote sensing and GIS*. Paper presented at the Recent Advances in Space Technologies, 2005. RAST 2005. Proceedings of 2nd International Conference on.

Clevers, J. G. P. W. (1989). Application of a weighted infrared-red vegetation index for estimating leaf Area Index by Correcting for Soil Moisture. *Remote Sensing of Environment, 29*(1), 25-37. doi: http://dx.doi.org/10.1016/0034-4257(89)90076-X

Clevers, J. G. P. W., & Kooistra, L. (2012). Using Hyperspectral Remote Sensing Data for Retrieving Canopy Chlorophyll and Nitrogen Content. *Selected Topics in Applied Earth Observations and Remote Sensing, IEEE Journal of, 5*(2), 574-583. doi: 10.1109/JSTARS.2011.2176468

Eitel, Jan UH, Keefe, Robert F, Long, Dan S, Davis, Anthony S, & Vierling, Lee A. (2010). Active ground optical remote sensing for improved monitoring of seedling stress in nurseries. *Sensors, 10*(4), 2843-2850.

Foody, Giles M., & Mathur, Ajay. (2006). The use of small training sets containing mixed pixels for accurate hard image classification: Training on mixed spectral responses for classification by a SVM. *Remote Sensing of Environment, 103*(2), 179-189. doi: http://dx.doi.org/10.1016/j.rse.2006.04.001

Gitelson, Anatoly A, Keydan, Galina P, & Merzlyak, Mark N. (2006). Three-band model for noninvasive estimation of chlorophyll, carotenoids, and anthocyanin contents in higher plant leaves. *Geophysical Research Letters, 33*(11).

Guyot, G, & Baret, F. (1988). *Utilisation de la haute resolution spectrale pour suivre l'etat des couverts vegetaux*. Paper presented at the Spectral Signatures of Objects in Remote Sensing.

Haboudane , D., Miller, J. R., Pattey, E., Strachan, I., & Zarco-Tejada, Pablo J. (2004). Hyperspectral vegetation indices and novel algorithms for predicting green LAI of crop canopies: modeling and validation in the context of precision agriculture.

Haboudane, Driss, Miller, John R., Tremblay, Nicolas, Zarco-Tejada, Pablo J., & Dextraze, Louise. (2002). Integrated narrow-band vegetation indices for prediction of crop chlorophyll content for application to precision agriculture. *Remote Sensing of Environment, 81*(2–3), 416-426. doi: http://dx.doi.org/10.1016/S0034-4257(02)00018-4

Hailu, Kassaye, R. (2006). *Suitability of Markov random field based method for super resolution land cover mapping*. ITC, Enschede. Retrieved from http://www.itc.nl/library/papers_2006/msc/gfm/hailu.pdf

Hatfield, Jerry L., & Prueger, John H. (2010). Value of Using Different Vegetative Indices to Quantify Agricultural Crop Characteristics at Different Growth Stages under Varying Management Practices. *Remote Sensing, 2*(2), 562-578.

Herries, G., Selige, T., & Danaher, S. (1996, 13 Feb 1996). *Singular value decomposition in applied remote sensing*. Paper presented at the Image Processing for Remote Sensing, IEE Colloquium on.

Hu, Y. H., Lee, H. B., & Scarpace, F. L. (1999). Optimal linear spectral unmixing. *Geoscience and Remote Sensing, IEEE Transactions on, 37*(1), 639-644. doi: 10.1109/36.739139
Huete, A. R. (1988). A soil-adjusted vegetation index (SAVI). *Remote Sensing of Environment, 25*(3), 295-309. doi: http://dx.doi.org/10.1016/0034-4257(88)90106-X
Jain, Namrata, Ray, ShibenduShankar, Singh, J. P., & Panigrahy, Sushma. (2007). Use of hyperspectral data to assess the effects of different nitrogen applications on a potato crop. *Precision Agriculture, 8*(4-5), 225-239. doi: 10.1007/s11119-007-9042-0
Kasetkasem, Teerasit, Arora, Manoj K., & Varshney, Pramod K. (2005). Super-resolution land cover mapping using a Markov random field based approach. *Remote Sensing of Environment, 96*(3–4), 302-314. doi: http://dx.doi.org/10.1016/j.rse.2005.02.006
Keshava, Nirmal. (2003). A survey of spectral unmixing algorithms. *Lincoln Laboratory Journal, 14*(1), 55-78.
Landgrebe, D.A. (2005). *Signal Theory Methods in Multispectral Remote Sensing*: Wiley.
Lelong, Camille C. D., Pinet, Patrick C., & Poilvé, Hervé. (1998). Hyperspectral Imaging and Stress Mapping in Agriculture: A Case Study on Wheat in Beauce (France). *Remote Sensing of Environment, 66*(2), 179-191. doi: http://dx.doi.org/10.1016/S0034-4257(98)00049-2
Li, S.Z. (2009). *Markov Random Field Modeling in Image Analysis*: Springer.
Liu, Jiangui, Pattey, Elizabeth, Miller, John R., McNairn, Heather, Smith, Anne, & Hu, Baoxin. (2010). Estimating crop stresses, aboveground dry biomass and yield of corn using multi-temporal optical data combined with a radiation use efficiency model. *Remote Sensing of Environment, 114*(6), 1167-1177. doi: http://dx.doi.org/10.1016/j.rse.2010.01.004
Melgani, F., & Bruzzone, L. (2004). Classification of hyperspectral remote sensing images with support vector machines. *Geoscience and Remote Sensing, IEEE Transactions on, 42*(8), 1778-1790. doi: 10.1109/TGRS.2004.831865
Mertens, K. C., Verbeke, L. P. C., Ducheyne, E. I., & De Wulf, R. R. (2003). Using genetic algorithms in sub-pixel mapping. *International Journal of Remote Sensing, 24*(21), 4241-4247. doi: 10.1080/0143116031000159507 3
National Research Council. (1997). *Precision Agriculture in the 21st Century: Geospatial and Information Technologies in Crop Management*: The National Academies Press.
Navarro-Cerrillo, Rafael Mª, Trujillo, Jesus, de la Orden, Manuel Sánchez, & Hernández-Clemente, Rocío. (2014). Hyperspectral and multispectral satellite sensors for mapping chlorophyll content in a Mediterranean Pinus sylvestris L. plantation. *International Journal of Applied Earth Observation and Geoinformation, 26*(0), 88-96. doi: http://dx.doi.org/10.1016/j.jag.2013.06.001
Neher, R., & Srivastava, A. (2005). A Bayesian MRF framework for labeling terrain using hyperspectral imaging. *Geoscience and Remote Sensing, IEEE Transactions on, 43*(6), 1363-1374. doi: 10.1109/TGRS.2005.846865
Poudyal, A. (2013). *Spatial statistics and super resolution mapping for precision agriculture using VHR satellite imagery*. University of Twente Faculty of Geo-Information and Earth Observation (ITC), Enschede. Retrieved from http://www.itc.nl/library/papers_2013/msc/gfm/poudyal.pdf
Quintano, Carmen, Fernández-Manso, Alfonso, Shimabukuro, Yosio E., & Pereira, Gabriel. (2012). Spectral unmixing. *International Journal of Remote Sensing, 33*(17), 5307-5340. doi: 10.1080/01431161.2012.661095
Rango, A., Laliberte, A., Herrick, J. E., Winters, C., Havstad, K., Steele, C., & Browning, D. (2009). Unmanned aerial vehicle-based remote sensing for rangeland assessment, monitoring, and management. *Journal of Applied Remote Sensing, 3*. doi: 10.1117/1.3216822
Rondeaux, Geneviève, Steven, Michael, & Baret, Frédéric. (1996). Optimization of soil-adjusted vegetation indices. *Remote Sensing of Environment, 55*(2), 95-107. doi: http://dx.doi.org/10.1016/0034-4257(95)00186-7
Schowengerdt, R. A. (1996). On the estimation of spatial-spectral mixing with classifier likelihood functions. *Pattern Recognition Letters, 17*(13), 1379-1387. doi: http://dx.doi.org/10.1016/S0167-8655(96)00094-3
Stagakis, Stavros, Markos, Nikos, Sykioti, Olga, & Kyparissis, Aris. (2010). Monitoring canopy biophysical and biochemical parameters in ecosystem scale using satellite hyperspectral imagery: An application on a Phlomis fruticosa Mediterranean ecosystem using multiangular CHRIS/PROBA observations. *Remote Sensing of Environment, 114*(5), 977-994. doi: http://dx.doi.org/10.1016/j.rse.2009.12.006

Suomalainen, J.M. , Anders, N.S., Iqbal, S., Franke, J., Wenting, P.F.M., Bartholomeus, H.M., . . . Kooistra, L. (2013). *A light-weight hyperspectral mapping system for Unmanned Aerial Vehicles – The first results.* Paper presented at the Proceedings of WHISPERS, 2013, Gainesville, Floroda, USA.

Tappen, M. F., & Freeman, W. T. (2003). *Comparison of graph cuts with belief propagation for stereo, using identical MRF parameters.* Paper presented at the Computer Vision, 2003. Proceedings. Ninth IEEE International Conference on.

Tatem, A. J., Lewis, H. G., Atkinson, P. M., & Nixon, M. S. (2001). Super-resolution target identification from remotely sensed images using a Hopfield neural network. *Geoscience and Remote Sensing, IEEE Transactions on, 39*(4), 781-796. doi: 10.1109/36.917895

Tatem, A. J., Lewis, H. G., Atkinson, P. M., & Nixon, M. S. (2003). Increasing the spatial resolution of agricultural land cover maps using a Hopfield neural network. *International Journal of Geographical Information Science, 17*(7), 647-672. doi: 10.1080/1365881031000135519

Tolpekin, V. A., & Stein, A. (2009). Quantification of the Effects of Land-Cover-Class Spectral Separability on the Accuracy of Markov-Random-Field-Based Superresolution Mapping. *Geoscience and Remote Sensing, IEEE Transactions on, 47*(9), 3283-3297. doi: 10.1109/TGRS.2009.2019126

Tso, B., & Mather, P.M. (2001). *Classification Methods for Remotely Sensed Data*: Taylor & Francis Group.

Tso, B., & Olsen, Richard C. (2005). A contextual classification scheme based on MRF model with improved parameter estimation and multiscale fuzzy line process. *Remote Sensing of Environment, 97*(1), 127-136. doi: http://dx.doi.org/10.1016/j.rse.2005.04.021

Verhoeye, Jan, & De Wulf, Robert. (2002). Land cover mapping at sub-pixel scales using linear optimization techniques. *Remote Sensing of Environment, 79*(1), 96-104. doi: http://dx.doi.org/10.1016/S0034-4257(01)00242-5

Wu, Jindong, Wang, Dong, Rosen, Carl J., & Bauer, Marvin E. (2007). Comparison of petiole nitrate concentrations, SPAD chlorophyll readings, and QuickBird satellite imagery in detecting nitrogen status of potato canopies. *Field Crops Research, 101*(1), 96-103. doi: http://dx.doi.org/10.1016/j.fcr.2006.09.014

Zhu, Honglei. (2005). Linear spectral unmixing assisted by probability guided and minimum residual exhaustive search for subpixel classification. *International Journal of Remote Sensing, 26*(24), 5585-5601. doi: 10.1080/01431160500181408

APPENDIX A

Data preparation

Spectral band position (nm)	Band width (nm)
490	7.3
530	8.5
550	9.2
570	9.7
670	11
700	12
710	12
740	13
750	13
780	11
870	12
940	13
950	13
1000	15
1050	15
1650	200

Table A.0.1: Specifications of Cropscan Multispectral radiometer. Source :(Clevers and Kooistra, 2012)

APPENDIX B

Relationship between Vegetation indices derived from super resolution image and field measurement.

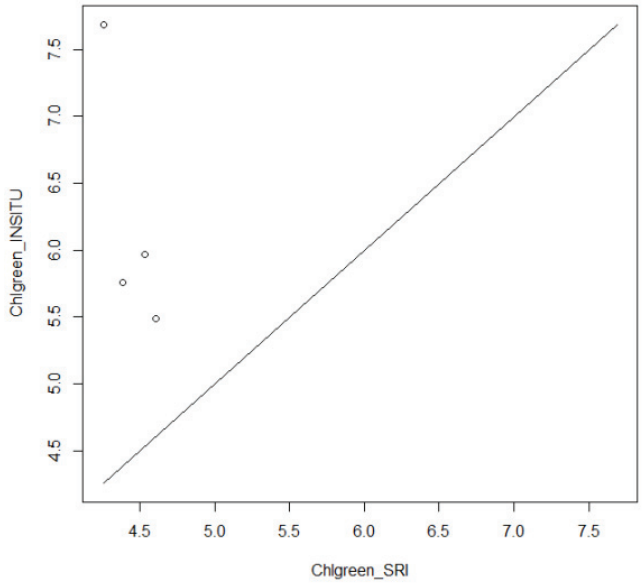

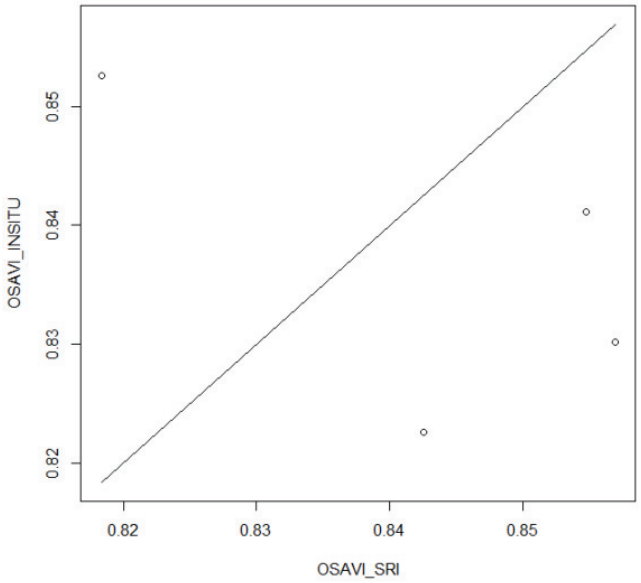

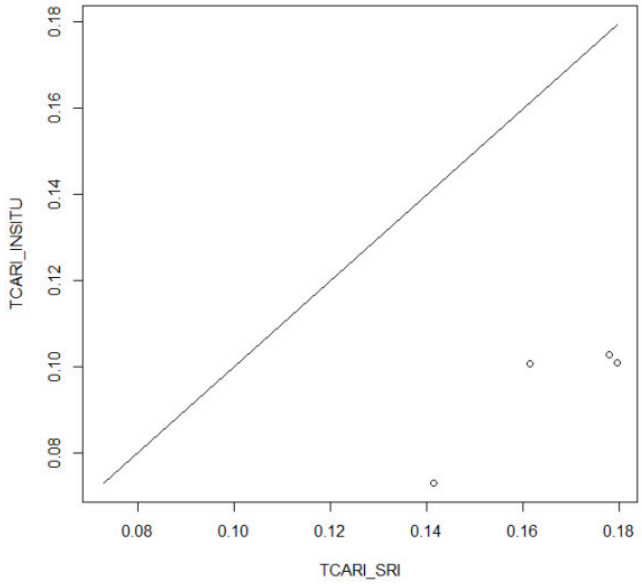

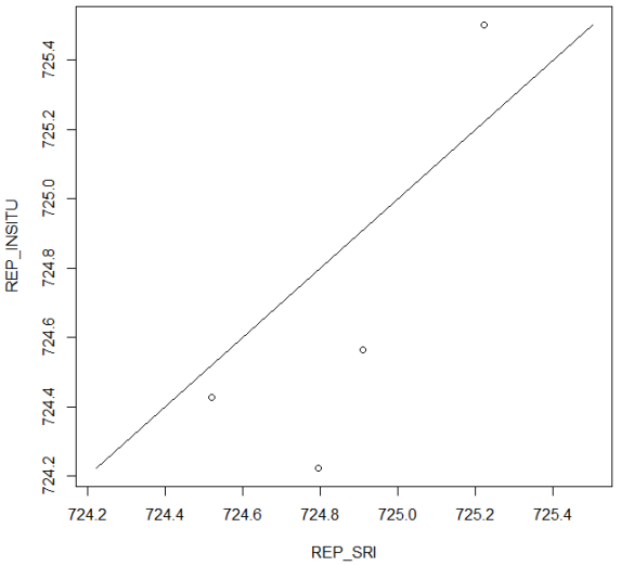

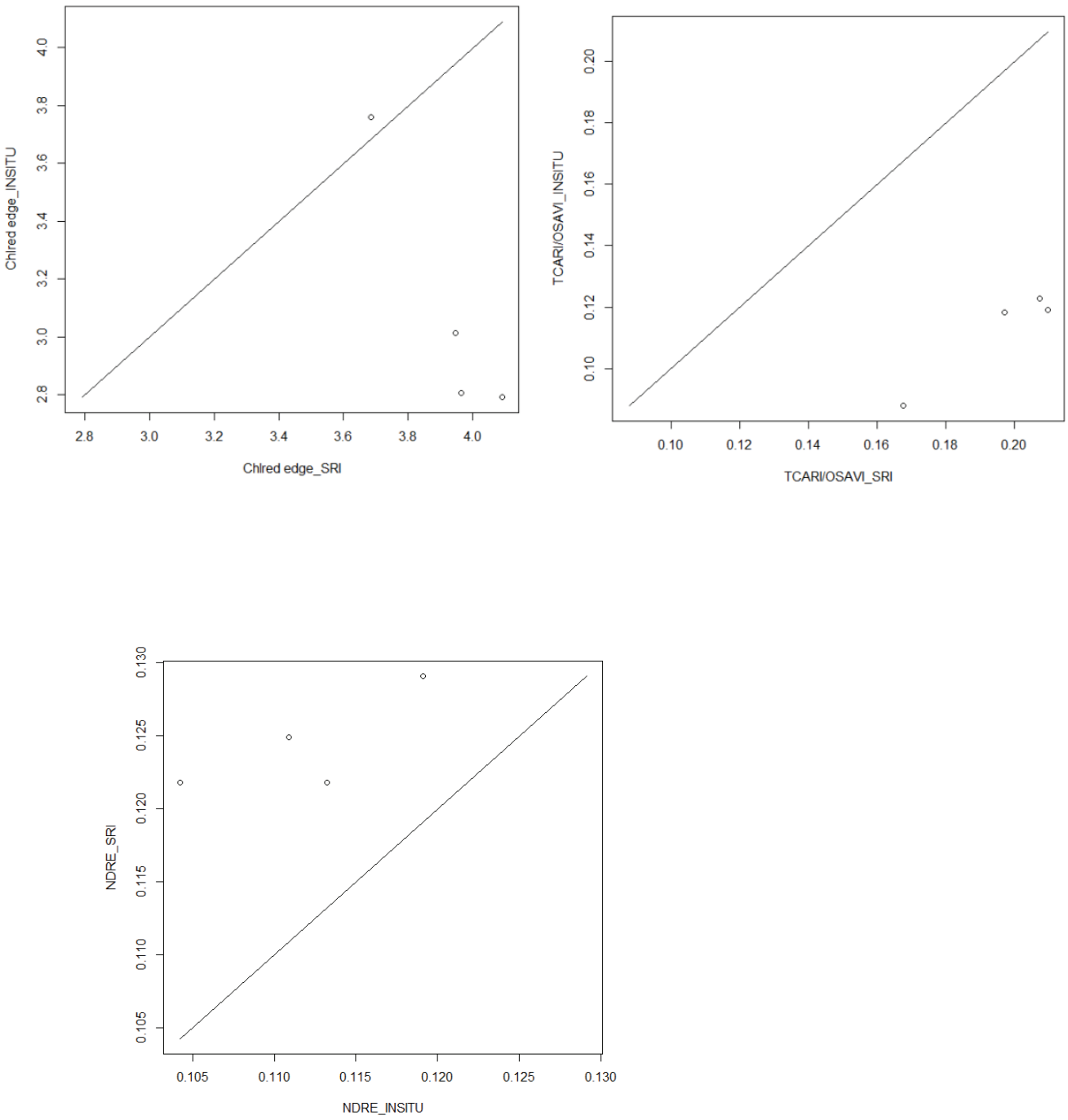

Figure B.0.1: Relationship between indices computed from the image and field data.